J. Fluid Mech. (1997), *vol.* 333, *pp.* 23–56

Numerical study of convection in the horizontal Bridgman configuration under the action of a constant magnetic field. Part 1. Two-dimensional flow

By HAMDA BEN HADID, DANIEL HENRY AND SLIM KADDECHE

Laboratoire de Mécanique des Fluides et d'Acoustique-UMR CNRS 5509, Ecole Centrale de Lyon/Université Claude Bernard-Lyon 1, ECL, BP 163, 69131 Ecully Cedex, France

(Received 6 December 1994 and in revised form 20 September 1996)

Studies of convection in the horizontal Bridgman configuration were performed to investigate the flow structures and the nature of the convective regimes in a rectangular cavity filled with an electrically conducting liquid metal when it is subjected to a constant vertical magnetic field. Under some assumptions analytical solutions were obtained for the central region and for the turning flow region. The validity of the solutions was checked by comparison with the solutions obtained by direct numerical simulations. The main effects of the magnetic field are first to decrease the strength of the convective flow and then to cause a progressive modification of the flow structure followed by the appearance of Hartmann layers in the vicinity of the rigid walls. When the Hartmann number is large enough, $Ha > 10$, the decrease in the velocity asymptotically approaches a power-law dependence on Hartmann number. All these features are dependent on the dynamic boundary conditions, e.g. confined cavity or cavity with a free upper surface, and on the type of driving force, e.g. buoyancy and/or thermocapillary forces. From this study we generate scaling laws that govern the influence of applied magnetic fields on convection. Thus, the influence of various flow parameters are isolated, and succinct relationships for the influence of magnetic field on convection are obtained. A linear stability analysis was carried out in the case of an infinite horizontal layer with upper free surface. The results show essentially that the vertical magnetic field stabilizes the flow by increasing the values of the critical Grashof number at which the system becomes unstable and modifies the nature of the instability. In fact, the range of Prandtl number over which transverse oscillatory modes prevail shrinks progressively as the Hartmann number is increased from zero to 5. Therefore, longitudinal oscillatory modes become the preferred modes over a large range of Prandtl number.

1. Introduction

In this paper we focus on the flow of an electrically conducting liquid metal contained in a differentially heated cavity subjected to a constant magnetic field. The flow which develops is of both buoyancy and thermocapillary origin. Buoyancy convection arises from the thermally induced density gradients and thermocapillary-driven flows from the thermally induced surface tension gradients at the free-liquid surface.

The flow field in such a configuration is of interest in a number of technological applications such as, for example, the production of crystals.

It has been recognized for many years that beyond a certain temperature difference between the vertical walls of the container a time-dependent flow (oscillatory then turbulent) appears. See for example Hurle, Jakeman & Johnson (1974), Carruthers (1977), Ben Hadid & Roux (1992), Pratte & Hart (1990), Hung & Andereck (1988, 1990). These time-dependent flows give rise to a fluctuating temperature field which in turn produces oscillatory crystal growth responsible for the microscopically non-uniform distribution of dopant in the crystal. When a magnetic field is imposed on an electrically conducting liquid, the liquid motion is reduced because of the interaction between the imposed magnetic field and the induced electric current. Therefore, the use of a magnetic field is considered to be an effective means for reducing or eliminating these undesired effects in electrically conducting liquids (see the review paper by Series & Hurle 1991), and thereby represents a promising method to improve crystal quality.

There are a number of modelling results on the effect of a constant magnetic field. Oreper & Szekely (1983, 1984), Motakef (1990) and Kim, Adornato & Brown (1988) used numerical simulation in a vertical Bridgman–Stockbarger configuration and demonstrated the dissipative influence of the applied magnetic field on the intensity of convection in the melt. More recently, Alboussière, Garandet & Moreau (1993) investigated analytically the influence of the cylinder cross-section shape on the core flow structure at large Hartmann number and concluded that with electric insulating walls, the magnetically damped convective velocity varies as Ha^{-2} when the cross-section has a horizontal plane of symmetry, while it varies as Ha^{-1} for non-symmetrical shapes. In the electrically conducting boundary case the trend of the velocity is of order Ha^{-2} and does not depend on the cross-section shape. A quantitative analysis of how an externally imposed magnetic field affects the impurities distribution was presented by Kaddeche, Ben Hadid & Henry (1994). Baumgartl & Müller (1992) investigated numerically the three-dimensional buoyancy-driven convection in a cylindrical geometry subjected to a constant magnetic field. Ozoe & Okada (1989) give numerical results for a differentially heated cubic box under the action of external magnetic fields.

The general equations governing the magnetohydrodynamic (MHD) flow are developed in §2 where particular mention is made of the Lorentz force term. In order to understand the full two-dimensional MHD flow behaviour a numerical model based upon the solution of the two-dimensional Navier–Stokes equations is adopted. The full set of MHD equations are nonlinear and prevent any sort of analytical progress being made on them. However, if certain simplifying assumptions are made, then it should be possible to find solutions which will exhibit realistic flow behaviour. The analytical model presented in §3 does serve to elucidate the likely behaviour of a fully developed flow in the case of an extended cavity $A \gg 1$ (A = length/height). An analytical treatment for the turning flow region is also proposed. A scaling analysis is presented in §4. In §5 the dependence of the velocity on the governing parameters (i.e. Grashof number Gr, Hartmann number Ha, and Reynolds number Re) is examined by use of direct numerical simulation and comparisons are made with derived analytical results. Finally, a résumé of the results obtained from the stability analysis of the extended cavity approximation is provided in §6.

2. Mathematical model and boundary conditions

2.1. *Governing equations*

A brief summary of the relevant equations used to describe laminar magnetohydrodynamic flow in a Bridgman configuration is now presented. The motion of an electrically conducting liquid in the presence of a magnetic field will give rise to a Lorentz force which acts on the fluid so that an extra body force term $\boldsymbol{F}$ appears in the Navier–Stokes equation. The Lorentz force term $\boldsymbol{F}$ in such a flow is given as follows:

$$\boldsymbol{F} = \rho_e \boldsymbol{E} + \boldsymbol{J} \times \boldsymbol{B}, \tag{2.1}$$

where ρ_e is the electric charge density of the fluid, $\boldsymbol{E} = -\nabla\phi$ the electric field intensity, ϕ the electric field potential, $\boldsymbol{J}$ the electric current density and $\boldsymbol{B}$ the magnetic field. On the other hand, the electric current density is described by Ohm's law for a moving medium:

$$\boldsymbol{J} = \rho_e \boldsymbol{v} + \sigma_e(-\nabla\phi + \boldsymbol{v} \times \boldsymbol{B}), \tag{2.2}$$

where σ_e is the electric conductivity and $\boldsymbol{v}$ the fluid velocity vector. In addition to the applied magnetic field $\boldsymbol{B}_0$, there is an induced magnetic field produced by the electric currents in the liquid metal. We assume in the following that the walls of the cavity are electric insulators and that the magnetic Reynolds number $Re_m = Pr_m Re_d$ is sufficiently small that the induced magnetic field is negligible with respect to the imposed constant magnetic field $\boldsymbol{B}_0$. Re_d is the dynamic Reynolds number, $Pr_m = \mu\sigma_e \nu$ the magnetic Prandtl number, μ the magnetic permeability and ν the kinematic viscosity. As ρ_e is very small in liquid metal, we can neglect the terms $\rho_e \boldsymbol{E}$ and $\rho_e \boldsymbol{v}$. For a Newtonian fluid the equations of motion and heat transport assuming the Boussinesq approximation may be written as:

$$\nabla \cdot \boldsymbol{v} = 0, \tag{2.3}$$

$$\frac{\partial \boldsymbol{v}}{\partial t} + (\boldsymbol{v} \cdot \nabla)\boldsymbol{v} = -\frac{1}{\rho_0}\nabla p + \nu\nabla^2 \boldsymbol{v} - [1 - \beta(T - T_0)]g\boldsymbol{e}_z + \frac{1}{\rho_0}\boldsymbol{J} \times \boldsymbol{B}_0, \tag{2.4}$$

$$\frac{\partial T}{\partial t} + (\boldsymbol{v} \cdot \nabla)T = \kappa\nabla^2 T, \tag{2.5}$$

where p denotes the pressure, β is the coefficient of thermal volumetric expansion, κ the thermal diffusivity and T_0 a reference temperature. Note that in equation (2.5) the viscous dissipation and Joule heating are neglected. Finally, from the conservation of electric current it follows that

$$\nabla \cdot \boldsymbol{J} = 0. \tag{2.6}$$

Equations (2.2) and (2.6) give an equation for ϕ:

$$\nabla^2 \phi = \nabla \cdot (\boldsymbol{v} \times \boldsymbol{B}_0). \tag{2.7}$$

2.2. *The two-dimensional model*

We consider a rectangular finite cavity of height H and length L (figure 1) filled with a low-Prandtl-number fluid of high conductivity. The upper horizontal boundary can be rigid, free or subject to a surface tension gradient. The flow developed in the fluid due to the horizontal thermal gradient resulting from differentially heated sidewalls is laminar. The surface tension on the free surface is a linear function of temperature and is given by $\sigma = \sigma_0[1 - \gamma(T - T_0)]$ where $\gamma = -(1/\sigma_0)(\partial\sigma/\partial T)$. In a two-dimensional formulation, if $\boldsymbol{B}_0$ is parallel to the plane of the cavity, (2.7) gives

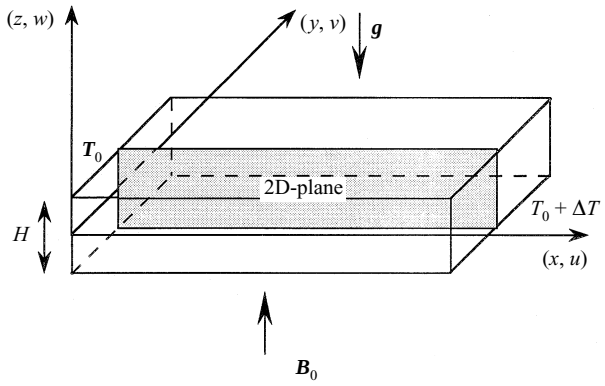

FIGURE 1. Schematic of the rectangular cavity. The left-hand and right-hand sidewalls are respectively cooled and heated.

$\nabla^2\phi = 0$, valid in the melt as well as in the neighbouring solid media. Since there is always somewhere around the enclosure an electrically insulating boundary on which $(\partial\phi/\partial n) = 0$, the unique solution is $\nabla\phi = 0$, which implies that the electric field vanishes everywhere. Then $\boldsymbol{J}$ reduces to $\sigma_e(\boldsymbol{v} \times \boldsymbol{B}_0)$ and the Lorentz force corresponds to a damping factor $\boldsymbol{F} = \sigma_e(\boldsymbol{v} \times \boldsymbol{B}_0) \times \boldsymbol{B}_0$.

The two-dimensional conservation equations of momentum and heat as used in the numerical procedure are made dimensionless using H, H^2/ν, ν/H and $\Delta T/A$ as scale quantities for, respectively, length, time, velocity and temperature. In these expressions, $A = L/H$ is the aspect ratio and $\Delta T = T_h - T_c$ the difference in temperature between the vertical sidewalls where T_h and T_c are the temperatures of the hot and cold walls, respectively. The dimensionless temperature θ is then $\theta = A(T - T_c)/\Delta T$, the vertical coordinate z is taken between -0.5 and 0.5 and the applied magnetic field is considered as purely vertical. The governing dimensionless equations in the melt in terms of a vorticity and stream function (ζ and ψ) formulation are

$$\frac{\partial\zeta}{\partial t} + \left[u\frac{\partial\zeta}{\partial x} + w\frac{\partial\zeta}{\partial z}\right] = \left[\frac{\partial^2\zeta}{\partial x^2} + \frac{\partial^2\zeta}{\partial z^2}\right] - Gr\frac{\partial\theta}{\partial x} - Ha^2\frac{\partial u}{\partial z}, \tag{2.8}$$

$$\left[\frac{\partial^2\psi}{\partial x^2} + \frac{\partial^2\psi}{\partial z^2}\right] - \zeta = 0, \tag{2.9}$$

with

$$u = \frac{\partial\psi}{\partial z}, \tag{2.10}$$

$$w = -\frac{\partial\psi}{\partial x}. \tag{2.11}$$

The heat transport equation is then

$$\frac{\partial\theta}{\partial t} + \left[u\frac{\partial\theta}{\partial x} + w\frac{\partial\theta}{\partial z}\right] = \frac{1}{Pr}\left[\frac{\partial^2\theta}{\partial x^2} + \frac{\partial^2\theta}{\partial z^2}\right]. \tag{2.12}$$

The associated boundary conditions are

$$x = 0: \qquad \psi = \frac{\partial\psi}{\partial z} = \frac{\partial\psi}{\partial x} = 0,\ \theta = 0, \tag{2.13a}$$

$$x = A: \qquad \psi = \frac{\partial \psi}{\partial z} = \frac{\partial \psi}{\partial x} = 0, \ \theta = A, \tag{2.13b}$$

$$z = -0.5: \qquad \psi = \frac{\partial \psi}{\partial z} = \frac{\partial \psi}{\partial x} = 0, \tag{2.13c}$$

and, for the rigid-rigid case,

$$z = 0.5: \qquad \psi = \frac{\partial \psi}{\partial z} = \frac{\partial \psi}{\partial x} = 0, \tag{2.13d}$$

whereas for the free surface case with surface tension effects,

$$z = 0.5: \qquad \psi = \frac{\partial \psi}{\partial x} = 0, \ \zeta = \frac{\partial^2 \psi}{\partial z^2} = -Re\frac{\partial \theta}{\partial x}. \tag{2.13e}$$

On the horizontal boundaries we consider two kinds of thermal conditions, either $\theta = x$ (conducting) or $(\partial\theta/\partial z) = 0$ (insulating).

The dimensionless parameters appearing in equations (2.8)–(2.13) are the Grashof number $Gr = g\beta\Delta T H^4/Lv^2$, the Reynolds–Marangoni number (called Reynolds number in the following) $Re = (-\partial\sigma/\partial T)\Delta T H^2/L\rho v^2$, the Prandlt number $Pr = v/\kappa$ and the Hartmann number $Ha = |\boldsymbol{B}_0|H(\sigma_e/\rho v)^{1/2}$.

3. Theoretical solutions

Theoretical solutions will be found for an infinite horizontal layer subjected to a horizontal temperature gradient. In such a two-dimensional layer the flow can be divided into three horizontal adjacent regions: the central region where the flow is horizontal and invariant, and the two end regions at $\pm$ infinity where the flow turns around. This simple model is a first tool for studying the interaction between the Lorentz force and the different driving forces of convection, i.e. buoyancy and thermocapillarity. A considerable simplification of the governing equations (2.8)–(2.12) is obtained. The rigid–rigid case has been treated by Garandet, Alboussière & Moreau (1992). We focus our study on the case with a free surface which can also be subjected to a surface tension force.

3.1. *One-dimensional mathematical model for the central region*

The dimensionless horizontal temperature gradient $(\partial\theta/\partial x)$ can be considered as constant and equal to one. The temperature is then taken as $\theta(x, z) = x + \theta_p(z)$. With these assumptions and in a one-dimensional approximation, (2.8)–(2.12) reduce to

$$\frac{\partial^3 u}{\partial z^3} - Ha^2\frac{\partial u}{\partial z} - Gr = 0, \tag{3.1}$$

$$\frac{\partial^2 \theta_p}{\partial z^2} = Pr\, u. \tag{3.2}$$

The solution of equation (3.1) for the velocity is of the form

$$u(z) = \frac{C_1}{Ha}\sinh(Ha(z+0.5)) + \frac{C_2}{Ha}\cosh(Ha(z+0.5)) - \frac{Gr}{Ha^2}(z+0.5) + C_3. \tag{3.3}$$

The coefficients C_1, C_2 and C_3 are determined by using the boundary conditions ($u(z = -0.5) = 0$ and $(\partial u/\partial z) = -Re$ on the upper free surface, i.e. $z = 0.5$) and the conservation of mass flow across any vertical plane in the liquid layer

($\int_{-0.5}^{0.5} u(z)\mathrm{d}z = 0$). We obtain the following three equations:

$$\frac{C_2}{Ha} + C_3 = 0, \tag{3.4a}$$

$$C_1 \cosh(Ha) + C_2 \sinh(Ha) - \frac{Gr}{Ha^2} = -Re, \tag{3.4b}$$

$$\frac{C_1}{Ha^2}(\cosh(Ha) - 1) + \frac{C_2}{Ha^2}\sinh(Ha) - \frac{Gr}{2Ha^2} + C_3 = 0, \tag{3.4c}$$

which give

$$C_1 = \frac{-HaK_1 + K_2 S}{S - HaC}, \quad C_2 = \frac{K_1 - K_2 C}{S - HaC}, \quad C_3 = \frac{-C_2}{Ha},$$

with $K_1 = -Re + \dfrac{Gr}{Ha^2}$, $K_2 = K_1 - \frac{1}{2}Gr$, $C = \cosh(Ha)$ and $S = \sinh(Ha)$.

Concerning the temperature, the solution θ_p to equation (3.2) is obtained by two successive integrations with respect to z: $\theta_p(z) = A + Bz + Pr\, f(z)$, with

$$f(z) = \frac{1}{Ha^2}\left(\frac{C_1}{Ha}\sinh(Ha(z+0.5)) + \frac{C_2}{Ha}\cosh(Ha(z+0.5)) - \frac{C_2}{Ha}\right) - \left(\frac{C_1}{Ha^2}(z+0.5) + \frac{Gr}{6Ha^2}(z+0.5)^3 + \frac{C_2}{2Ha}(z+0.5)^2\right), \tag{3.5}$$

where A and B are integration constants. Depending on the thermal boundary conditions, different solutions can be obtained:
conducting conditions: $\theta_p(z) = Pr[f(z) - (z+0.5)f(0.5)]$,
insulating conditions: $\theta_p(z) = Pr[f(z) - \int_{-0.5}^{0.5} f(z)\mathrm{d}z]$.

In the low-Ha limit, power series expansions of these expressions for the velocity and the temperature give the characteristic profiles obtained in the absence of a magnetic field. In the high-Ha range an asymptotic expression, valid in the whole cavity, can be found for the velocity:

$$u(z) = -\frac{Gr}{Ha^2}z - \frac{K_1}{Ha^2} + \frac{K_1}{Ha}\mathrm{e}^{-Ha(-z+0.5)} + \frac{K_2}{Ha^2}\mathrm{e}^{-Ha(z+0.5)}. \tag{3.6}$$

This gives the following simplified expressions:
in the core,

$$u(z) = -\frac{Gr}{Ha^2}z + \frac{Re}{Ha^2} + O(Ha^{-4}), \tag{3.7a}$$

and at the upper surface,

$$u(0.5) = -\frac{Re}{Ha} - \frac{Gr}{2Ha^2} + \frac{Re}{Ha^2} + O(Ha^{-3}). \tag{3.7b}$$

With buoyancy forces ($Gr \neq 0$), the influence of the Hartmann number Ha is displayed in figure 2 where it is apparent that the profile of the horizontal component of velocity tends to a constant vertical gradient (with a Ha^{-2} variation) almost everywhere in the cavity except in the thin Hartmann layer of thickness Ha^{-1} near the bottom wall where the classical Hartmann exponential profile holds. With thermocapillary forces ($Re \neq 0$), the horizontal component of the velocity, displayed in figure 3, has a large

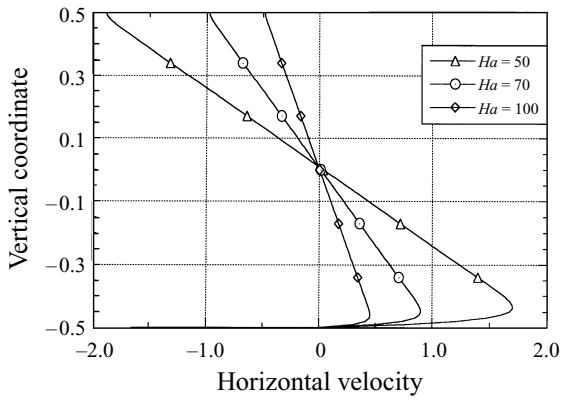

FIGURE 2. Vertical profiles of the horizontal velocity. Analytical solution (3.3) in the rigid–free case for pure buoyancy effect ($Gr = 10^4$, $Re = 0$) for three values of the Hartmann number ($Ha = 50$, 70 and 100).

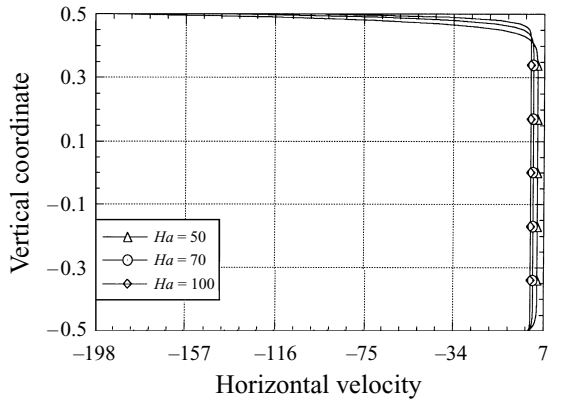

FIGURE 3. As figure 2 but for pure thermocapillary effect ($Gr = 0$, $Re = 10^4$).

value at the surface (Ha^{-1} variation), whereas the recirculation in the core occurs in almost the whole volume with a constant profile (Ha^{-2} variation), a thin Hartmann layer allowing the transition to the zero flow velocity at the bottom wall. Note that most of these features are clearly expressed through the expression (3.6). When both forces are combined, an intermediate behaviour is obtained depending on the value of the Bond number $Bd = Gr/Re$. The variations of the horizontal velocity profile as a function of the magnetic field intensity (given by Ha) are shown in figure 4 for two cases corresponding to the combined action of buoyancy forces ($Gr = 6000$) and thermocapillary forces ($Re = 10^4$ and 10^2). Noteworthy is the variation of the velocity profiles as Re is increased, corresponding to an increase of the Bond number from 0.6 to 60. Differences are particularly noticeable when Ha values are high.

In fact, equation (3.1) shows that in the core where the viscosity is negligible, the curl of the Lorentz force with magnitude $-Ha^2(\partial u/\partial z)$ vanishes in the case of surface forces whereas it is constant in the case of buoyancy forces. This leads to the two types of profiles mentioned above: an even velocity profile with constant value and an odd profile with constant gradient, respectively.

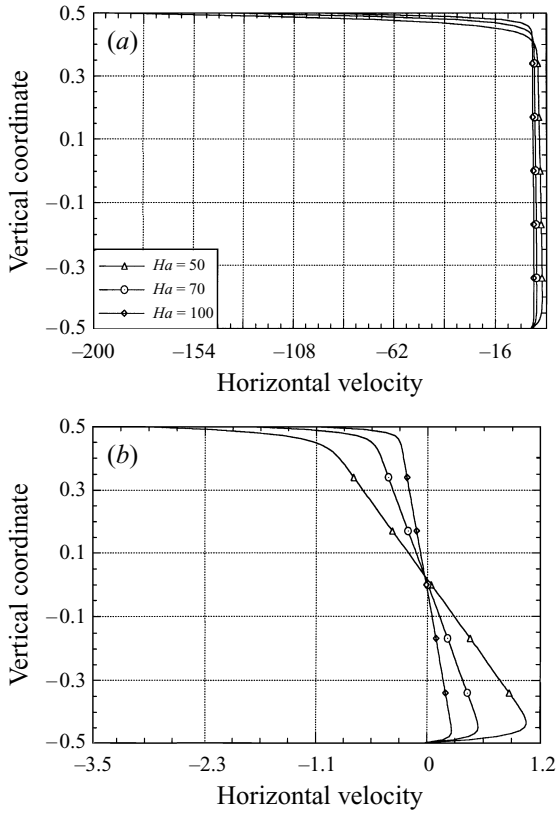

FIGURE 4. Vertical profiles of the horizontal velocity. Analytical solution (3.3) in the rigid–free case for buoyancy and thermocapillary effects for $Gr = 6 \times 10^3$ and three values of the Hartmann number ($Ha = 50$, 70 and 100): (*a*) $Re = 10^4$ ($Bd = 0.6$); (*b*) $Re = 10^2$ ($Bd = 60$).

The asymptotic expression obtained for the temperature in the high-Ha range is

$$f(z) = -\frac{Gr}{6Ha^2}(z+0.5)^3 + \frac{K_2}{Ha^2}\left(-\frac{(z+0.5)^2}{2} + \frac{(z+0.5)}{Ha} - \frac{1}{Ha^2}\right) + \frac{K_1}{Ha^3}\mathrm{e}^{-Ha(-z+0.5)} + \frac{K_2}{Ha^4}\mathrm{e}^{-Ha(z+0.5)}. \tag{3.8}$$

This gives the following simplified expressions:
in the core,

$$f(z) = \frac{Gr}{2Ha^2}\left(\frac{(z+0.5)^2}{2} - \frac{(z+0.5)^3}{3}\right) + \frac{Re}{Ha^2}\frac{(z+0.5)^2}{2} + O(Ha^{-3}), \tag{3.9a}$$

and at the upper surface,

$$f(0.5) = \frac{Gr}{12Ha^2} + \frac{Re}{2Ha^2} + O(Ha^{-3}). \tag{3.9b}$$

From relations (3.9) it is clear that the temperature profiles are all of $O(Ha^{-2})$. These profiles, which are displayed in figure 5 for both conducting and insulating thermal conditions, correspond to cubic curves with buoyancy forces (figure 5*a*, *b*) and parabolic curves with thermocapillary forces (figure 5*c*, *d*). From the latter we notice that even with surface forces there is a continuity between the results in the core

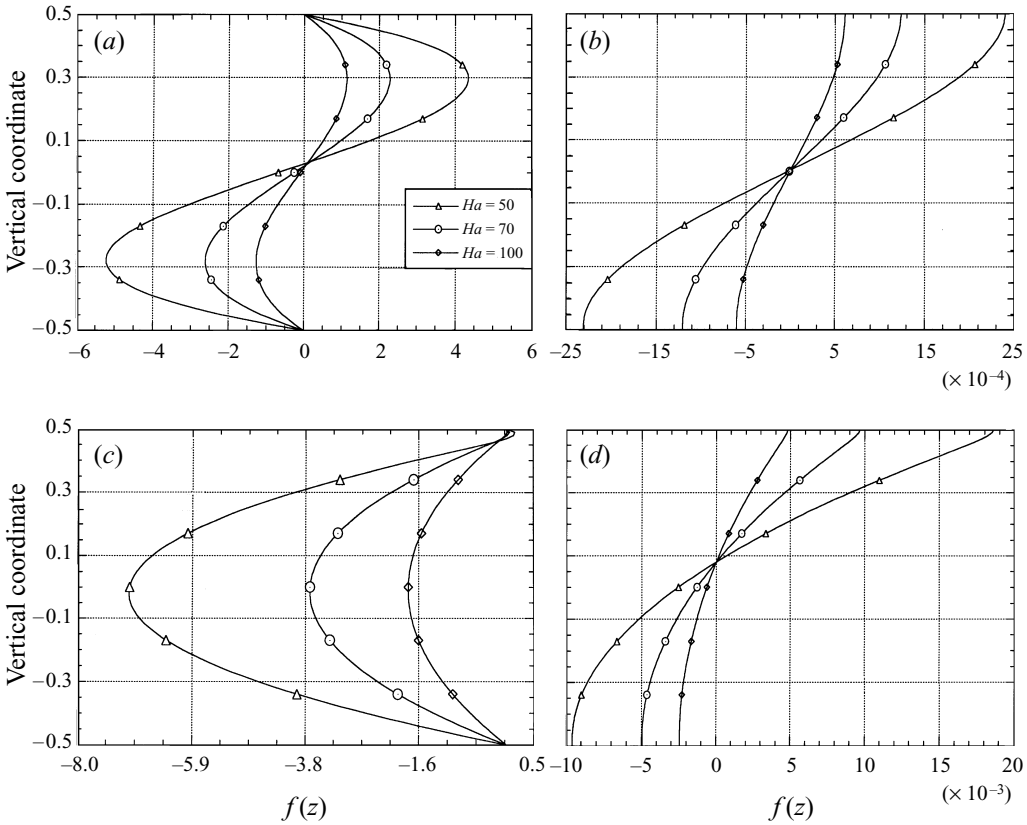

FIGURE 5. Vertical profiles of the temperature given by $f(z)$. Analytical solution (3.5) in the rigid–free case for $Ha = 50$, 70 and 100, for buoyancy or thermocapillary effect and different thermal boundary conditions. (*a*) Conducting case, $Gr = 10^4$, $Re = 0$; (*b*) insulated case, $Gr = 10^4$, $Re = 0$; (*c*) conducting case, $Gr = 0$, $Re = 10^4$; (*d*) insulated case, $Gr = 0$, $Re = 10^4$.

and at the surface. The temperature profiles are mainly affected by the core velocity and the strong surface velocity of $O(Ha^{-1})$ has no important effect on them. In fact, during the two integrations performed to obtain θ_p, the dominant term of $O(Ha^{-1})$ for the surface velocity leads to only a negligible term of $O(Ha^{-3})$ in the temperature.

3.2. *The turning flow region*

Here we consider the analytical calculation of the turning flow by considering a semi-infinite cavity from $x = 0$ (corresponding to one of the endwalls) to infinity with a fluid layer between $z = -0.5$ and 0.5. If we neglect the inertial terms, which can be expected to be a good approximation in the high-Ha range as the velocities have just been found to decrease strongly, the equation of motion (2.8) can be written in the following form:

$$\left[\frac{\partial^2\zeta}{\partial x^2} + \frac{\partial^2\zeta}{\partial z^2}\right] - Gr\frac{\partial\theta}{\partial x} - Ha^2\frac{\partial u}{\partial z} = 0. \tag{3.10}$$

We now consider that the temperature gradient is still constant in these recirculating zones, i.e. the convective heat transfer is negligible. This hypothesis is realistic in the high Ha range, especially in the case of a low Prandtl number fluid. Recasting

equation (3.10) using the definition of the vorticity (2.9), we obtain the following equation for ψ:

$$\nabla^4\psi - Ha^2\frac{\partial^2\psi}{\partial z^2} = Gr. \tag{3.11}$$

The associated boundary conditions are those defined in (2.13) for $x = 0$, $z = -0.5$ and $z = 0.5$. Moreover the different variables must be finite as z tends towards infinity.

We can seek a solution in the form of a Fourier series expansion in z. In order to satisfy the boundary condition for the thermocapillary case, we must add a polynomial expansion in z. The expansion is then taken as follows:

$$\psi = \sum_{j=0}^{\infty} V_j(x)\cos(\alpha_j z) + \sum_{k=0}^{\infty} W_k(x)\sin(\gamma_k z) - \tfrac{1}{6}Re((z^2 - \tfrac{1}{4})(z + \tfrac{3}{2})), \tag{3.12}$$

with $\alpha_j = (2j+1)\pi$, $j = 0, \infty$ and $\gamma_k = 2(k+1)\pi$, $k = 0, \infty$.
Equation (3.12) satisfies all the conditions at the horizontal boundaries, except the no-slip condition at $z = -0.5$, i.e. the Hartmann layer near the bottom wall is not considered. This approximation is not too drastic as the Hartmann layer has here a passive nature (the electric current in the core is not forced to close in this layer). Moreover, the classical exponential variation of the velocity distribution within the Hartmann layers (see (3.6)) could be used to satisfy the realistic no-slip condition, at least when Ha is large.

If we put this expansion into equation (3.11), expand the polynomial in the sine and cosine bases, and use the orthogonality of the sine and cosine functions, we obtain equations for V_j and W_k that have to be solved with the appropriate boundary conditions. After some tedious calculations which are presented in Appendix, we obtain the solutions for ψ, u and w, given for ψ by (3.12), and for u and w by the following expressions:

$$u = \frac{\partial\psi}{\partial z} = -\sum_{j=0}^{\infty} V_j(x)\alpha_j\sin(\alpha_j z) + \sum_{k=0}^{\infty} W_k(x)\gamma_k\cos(\gamma_k z) - \tfrac{1}{6}Re((z^2 - \tfrac{1}{4}) + 2z(z + \tfrac{3}{2})), \tag{3.13}$$

$$w = -\frac{\partial\psi}{\partial x} = -\sum_{j=0}^{\infty} V_j'(x)\cos(\alpha_j z) - \sum_{k=0}^{\infty} W_k'(x)\sin(\gamma_k z). \tag{3.14}$$

with

$$V_j(x) = \lambda_j e^{-a_j x}\cos(b_j x) + \mu_j e^{-a_j x}\sin(b_j x) + \frac{g_j}{(\alpha_j^4 + Ha^2\alpha_j^2)},$$

$$V_j'(x) = -e^{-a_j x}(b_j\lambda_j + a_j\mu_j)\sin(b_j x),$$

and

$$W_k(x) = \nu_k e^{-c_k x}\cos(d_k x) + \pi_k e^{-c_k x}\sin(d_k x) + \frac{h_k}{(\gamma_k^4 + Ha^2\gamma_k^2)},$$

$$W_k'(x) = -e^{-c_k x}(d_k\nu_k + c_k\pi_k)\sin(d_k x),$$

where

$$\lambda_j = V_{j0} - \frac{g_j}{(\alpha_j^4 + Ha^2\alpha_j^2)}, \quad \mu_j = \frac{a_j}{b_j}\lambda_j,$$

and

$$v_k = W_{k0} - \frac{h_k}{(\gamma_k^4 + Ha^2\gamma_k^2)}, \quad \pi_k = \frac{c_k}{d_k} v_k.$$

We have also

$$V_{j0} = -Re\frac{2(-1)^j}{\alpha_j^3} \quad \text{and} \quad W_{k0} = -Re\frac{2(-1)^k}{\gamma_k^3},$$

with

$$g_j = (-Ha^2\tfrac{1}{2}Re + Gr)\frac{4(-1)^j}{\alpha_j} \quad \text{and} \quad h_k = -Ha^2 Re\frac{2(-1)^k}{\gamma_k}.$$

Finally,

$$a_j = \frac{1}{\sqrt{2}}\left(\alpha_j^2 + \alpha_j(Ha^2 + \alpha_j^2)^{1/2}\right)^{1/2} \quad \text{and} \quad b_j = \frac{1}{\sqrt{2}}\left(-\alpha_j^2 + \alpha_j(Ha^2 + \alpha_j^2)^{1/2}\right)^{1/2},$$

$$c_k = \frac{1}{\sqrt{2}}\left(\gamma_k^2 + \gamma_k(Ha^2 + \gamma_k^2)^{1/2}\right)^{1/2} \quad \text{and} \quad d_k = \frac{1}{\sqrt{2}}\left(-\gamma_k^2 + \gamma_k(Ha^2 + \gamma_k^2)^{1/2}\right)^{1/2}.$$

We can derive the expressions valid in the high-Ha range. If we suppose that $Ha \gg \alpha_j$ and $Ha \gg \gamma_k$, that is, more precisely, that Ha is greater than each α_j and γ_k which plays a significant role in the expansion, we can write

$$a_j \sim b_j \sim (\tfrac{1}{2}Ha\alpha_j)^{1/2} \quad \text{and} \quad c_k \sim d_k \sim (\tfrac{1}{2}Ha\gamma_k)^{1/2}.$$

Moreover

$$V_{j\infty} = \frac{g_j}{\alpha_j^4 + Ha^2\alpha_j^2} = -Re\frac{2(-1)^j}{\alpha_j^3} + Gr\frac{4(-1)^j}{\alpha_j^3 Ha^2} + Re\frac{2(-1)^j}{\alpha_j Ha^2} + O(Ha^{-4}),$$

$$W_{k\infty} = \frac{h_k}{\gamma_k^4 + Ha^2\gamma_k^2} = -Re\frac{2(-1)^k}{\gamma_k^3} + Re\frac{2(-1)^k}{\gamma_k Ha^2} + O(Ha^{-4}),$$

and

$$\mu_j \sim \lambda_j = V_{j0} - V_{j\infty}, \quad \pi_k \sim \nu_k = W_{k0} - W_{k\infty}.$$

In order to check the consistency of our approach with respect to the solution in the central region calculated in §3.1, we can express the results as x tends towards infinity in the high-Ha range. Since $V_j(x) \to V_{j\infty}$ and $W_k(x) \to W_{k\infty}$, we have

$$\psi = \sum_{j=0}^{\infty}\left(-Re\frac{2(-1)^j}{\alpha_j^3} + Gr\frac{4(-1)^j}{\alpha_j^3 Ha^2} + Re\frac{2(-1)^j}{\alpha_j Ha^2}\right)\cos(\alpha_j z)$$
$$+ \sum_{k=0}^{\infty}\left(-Re\frac{2(-1)^k}{\gamma_k^3} + Re\frac{2(-1)^k}{\gamma_k Ha^2}\right)\sin(\gamma_k z) - \tfrac{1}{6}Re((z^2 - \tfrac{1}{4})(z + \tfrac{3}{2})) + O(Ha^{-4}).$$

By using the expansions of the polynomials given in the Appendix, we can find the expressions corresponding to the above expansions:

$$\psi_\infty \sim \frac{-Gr}{2Ha^2}(z^2 - \tfrac{1}{4}) + \frac{Re}{Ha^2}(z + \tfrac{1}{2}),$$

and

$$v_\infty \sim -z\frac{Gr}{Ha^2} + \frac{Re}{Ha^2}. \tag{3.15}$$

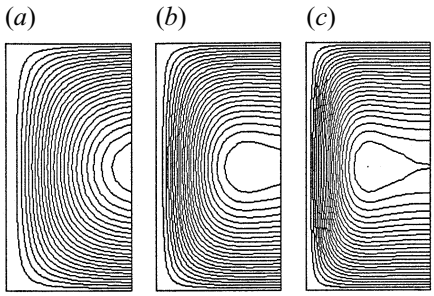

FIGURE 6. Streamlines giving the structure of the turning flow near the endwalls. Analytical solution (3.12) obtained by means of Fourier expansion in the rigid–free case for pure buoyancy effect ($Gr = 10^4$, $Re = 0$) and (*a*) $Ha = 10$; (*b*) $Ha = 50$; (*c*) $Ha = 100$.

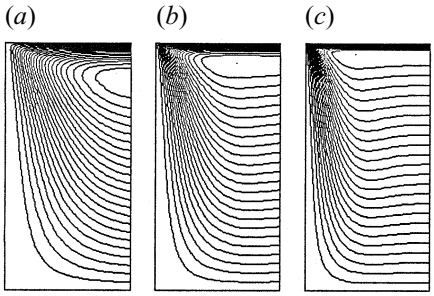

FIGURE 7. As figure 6 but for pure thermocapillary effect ($Gr = 0$, $Re = 10^4$).

We get then an expression for v_∞ identical to the one obtained in the core with the monodimensional model (3.7*a*). Moreover, by directly using the expressions (3.12) and (3.13) for large x with enough terms in the expansion, we obtain streamfunction and velocity profiles in the high-Ha range approximately similar to those of the monodimensional model, except for the Hartmann layer at the bottom of the cavity which is not taken into account in the present model.

The structure of the turning flow near the endwalls is displayed in figure 6 for the pure buoyancy case ($Gr = 10^4$, $Re = 0$), and in figure 7 for the pure thermocapillary case ($Gr = 0$, $Re = 10^4$) by means of streamlines for three values of the Hartmann number, 10, 50 and 100. In the buoyancy case, figure 6 shows the decrease of the boundary layer near the endwall as Ha is increased, and the appearance of a small recirculation cell at the centre of the turning flow. In the thermocapillary case, figure 7 shows, as will be confirmed by the direct numerical simulation results, a marked asymmetry of the flow with the formation of a fluid layer at the surface which becomes thinner and thinner as the Hartmann number is increased. Near the endwall, a boundary layer is formed whose thickness is variable with the depth for high values of Ha. The structure of the turning flow near the end of the cavity for three Bond numbers $Bd = 60$, 6 and 0.6 is displayed in figure 8 for fixed Grashof number ($Gr = 6 \times 10^3$) and Hartmann number ($Ha = 100$). From the figure it is clear that the flow structures for the two limit cases, i.e. $Bd = 60$ and 0.6, are almost similar to the pure buoyancy case and pure thermocapillary case, respectively, while $Bd = 6$ gives an intermediate structure.

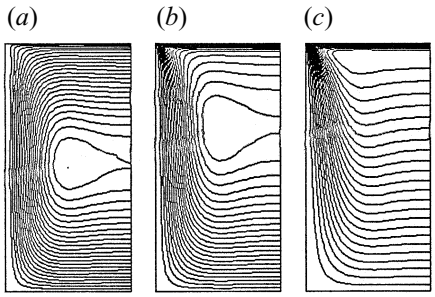

FIGURE 8. As figure 6 but for $Ha = 100, Gr = 6 \times 10^3$ with buoyancy and thermocapillary effects: (*a*) $Re = 10^2$ ($Bd = 60$); (*b*) $Re = 10^3$ ($Bd = 6$); (*c*) $Re = 10^4$ ($Bd = 0.6$).

4. Scaling analysis

The characteristic behaviours for large Ha can also be obtained by a scaling analysis. We can make use of the vorticity equation (3.10) with $(\partial\theta/\partial x) = 1$ or of the equation of ψ (3.11). For a shallow cavity, in the central region the flow is unidirectional ($w = 0$) and independent of x.

4.1. *Boundary layers*

We can derive the characteristic lengths corresponding to the Hartmann layer (δ_{Ha}) and to the parallel layer ($\delta_{\|}$). For that, we use (3.11) and, as the term on the right-hand side does not depend on boundary layer thickness, we make the two terms of the left-hand side equal.

For the Hartmann layers along the horizontal boundaries, the relevant length scale for both viscous and magnetic terms is $\delta_z = \delta_{Ha}$, δ_x being of order unity. We get then $(1/\delta_{Ha}^4) \sim (Ha^2/\delta_{Ha}^2)$, and so

$$\delta_{Ha} \sim Ha^{-1}. \tag{4.1}$$

For the parallel layers along the vertical boundaries, the relevant length scale for the viscous term is $\delta_x = \delta_{\|}$ and that for the magnetic term is δ_z of order unity. We get then $(1/\delta_{\|}^4) \sim (Ha^2/1)$, and so

$$\delta_{\|} \sim Ha^{-1/2}. \tag{4.2}$$

4.2. *Rigid–rigid cavity*

In the central region, the motion is driven by buoyancy-induced pressure gradient and the velocity profile, u, has a Z-like shape (Garandet *et al.* 1992). Outside the boundary layers of size $\delta_z = \delta_{Ha}$ (i.e. $-0.5 + \delta_z \leqslant z \leqslant 0.5 - \delta_z$), the viscous effects are small and the dominant balance occurs between the Lorentz term and the buoyancy term, which leads (with $(\partial u/\partial z) \sim (u/1)$) in (3.10) to a horizontal velocity scale $u \sim GrHa^{-2}$.

Near the endwalls, the fluid flows with a mean vertical velocity w throughout a layer of thickness $\delta_x = \delta_{\|}$. Since there is only one global circulation roll, this heated fluid will travel horizontally along the top wall of the cavity in a layer of thickness $1/2$ (or $H/2$ in dimensional form). The continuity between the vertical and horizontal circulations gives $w\,\delta_x \sim u$, and so $w \sim GrHa^{-3/2}$.

From the above analyses, we can state that for large Hartmann numbers $Ha > 10$, the maximum values of u and w are

$$u_{max} \sim GrHa^{-2} \tag{4.3}$$

and

$$w_{max} \sim GrHa^{-3/2}, \tag{4.4}$$

and the associated length scales on z and x are, respectively, 1 and $Ha^{-1/2}$. Considering the equation in primitive variables, the Lorentz force ($Ha^2 u$) is then of order Gr, and the leading contribution to the inertial term $(\boldsymbol{v}\cdot\nabla)\boldsymbol{v}$ varies like $Gr^2 Ha^{-3}$. A condition for inertia term to be negligible thus is

$$Ha^3 \gg Gr. \tag{4.5}$$

4.3. *Rigid–free cavity*

In the pure buoyancy case, the characteristic variations are similar to those of the rigid–rigid cavity and can be obtained by analogous considerations. The only difference is the absence of a real Hartmann layer at the upper free boundary.

In the pure thermocapillary case, the entire flow is driven by temperature-induced surface tension gradients at the upper surface. Large velocities are then created at this upper surface and drive the subsurface layer of thickness δ_z. The scaling law at this upper surface is determined by the balance between shear and thermocapillary forces as expressed by the thermocapillary boundary condition (2.13*e*). Thus, we obtain $u \sim Re\,\delta_z$.

In the subsurface layer, for large Hartmann numbers the correct balance is between viscous and magnetic forces. Inserting $Gr = 0$, $(\partial^2\zeta/\partial x^2) = 0$ and $\zeta \sim u/\delta_z$ in (3.10), gives $\delta_z \sim Ha^{-1}$ and so $u \sim ReHa^{-1}$, establishing that the upper circulation will occur inside the Hartmann layer.

The scaling law for the constant returning core velocity which applies on almost the whole height of the cavity (except the boundary layers) can be obtained from the mass conservation equation. We find $u_{ret} \sim ReHa^{-2}$.

Near the endwalls, the fluid flows with a mean vertical velocity w throughout a layer of thickness $\delta_x = \delta_\parallel$. The continuity with the horizontal circulations give $w \sim ReHa^{-3/2}$.

Finally, for large Hartmann numbers, the maximum values of the horizontal and vertical velocities are, respectively,

$$u_{max} \sim ReHa^{-1} \tag{4.6}$$

and

$$w_{max} \sim ReHa^{-3/2}, \tag{4.7}$$

and the associated length scales on z and x are, respectively, Ha^{-1} and $Ha^{-1/2}$. The Lorentz force is then of order $ReHa$, and the leading contributions to the inertial terms vary like $Re^2 Ha^{-3/2}$. The condition for inertial terms to be negligible thus becomes

$$Ha^{5/2} \gg Re. \tag{4.8}$$

5. Numerical results

The numerical scheme employed is based upon a highly accurate method which has proven effective for classical hydrodynamical problems. The technique employed to solve the system of non-dimensionalized equations (2.8)–(2.13) was the culmination of earlier work on accurate numerical representations of Navier–Stokes and energy equations (Roux *et al.* 1979 and Ben Hadid 1989). The main features of this numerical technique are:

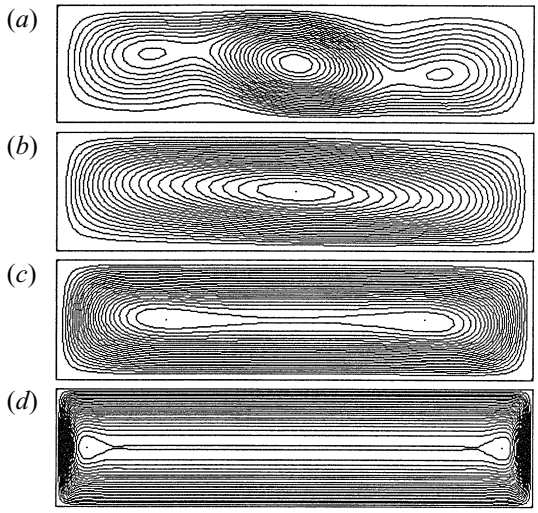

FIGURE 9. Streamlines giving the structure of the flow in the cavity. Results obtained in the rigid–rigid case for buoyancy effect ($Gr = 2 \times 10^4$) and (*a*) $Ha = 0$; (*b*) $Ha = 5$; (*c*) $Ha = 10$; (*d*) $Ha = 100$.

(i) an alternating direction implicit (ADI) method for solving the finite-difference equations (2.8), (2.9) and (2.12),

(ii) a second-order central differentiation for spatial derivatives for (2.8) and (2.12),

(iii) a fourth-order compact Hermitian method for (2.9).

The Hermitian approach is based upon the use of the variables, the first derivatives and the second derivatives as unknowns. The block-tridiagonal matrix inversion algorithm (Thomas algorithm), resulting from the use of high-order Hermitian finite-difference relationships, was employed for (2.9). The vorticity at the boundary was calculated with the third-order relationship (known in the literature as Hirsh's relationship) and already used for natural convection problems by Roux *et al.* (1979) and Ben Hadid (1989). The convergence criterion was based on the vorticity variation at the boundary and a solution of the system of equations (2.8)–(2.13) is considered to be converged when the variation of the (reduced) vorticity at the boundary is less than 0.01%. The mesh used to solve the problem is generated by the Thompson technique (Thompson, Thames & Mastin 1974). We used for calculations in cavities with an aspect ratio $A = 4$ a 31×101 symmetric grid for the rigid–rigid case and a 35×121 grid for the rigid–free and thermocapillary cases. In both cases the grid was concentrated near the walls and the free surface. The grid size is gradually increased away from the boundaries with the finest grid size being about three and half times smaller than the one corresponding to the uniform grid. Note that this grid refinement ensures that the Hartmann layers are well resolved in all cases.

The two-dimensional results concern a rigid–rigid cavity and a cavity with a free surface and are presented by plotting streamlines and velocity profiles. In the present study the Prandtl number was constant and equal to 0.01, characteristic of liquid metals and semiconductors. In a cavity with a free surface the fluid flow is driven by the combined action of buoyancy and thermocapillary forces. Each of these two cases of buoyancy-driven flow and thermocapillary-driven flow is considered separately. We also analyse their combined effects in terms of Bond number.

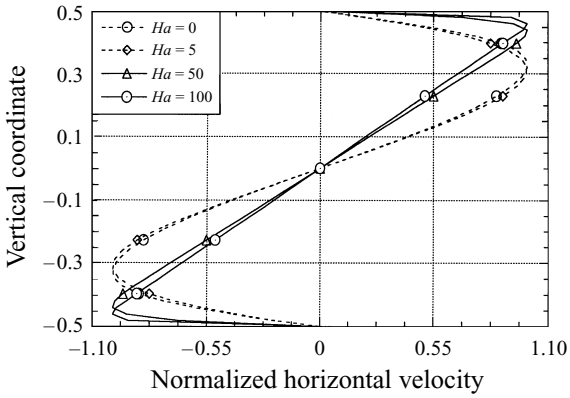

FIGURE 10. Vertical profiles of the normalized horizontal velocity at mid-length of the cavity. Results obtained by numerical simulation in the rigid–rigid case for buoyancy effect ($Gr = 2 \times 10^4$) and $Ha = 0$, 5, 50 and 100.

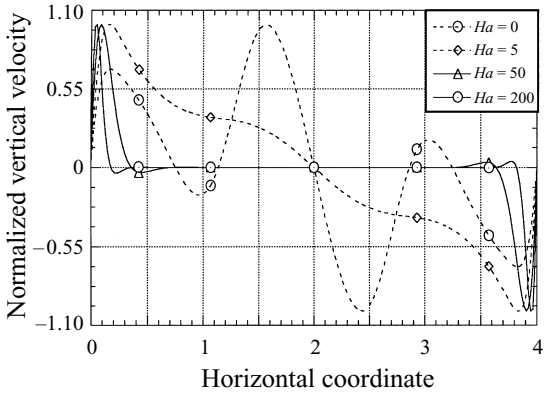

FIGURE 11. Horizontal profiles of the normalized vertical velocity at mid-height of the cavity. Results obtained by numerical simulation in the rigid–rigid case for buoyancy effect ($Gr = 2 \times 10^4$) and $Ha = 0$, 5, 50 and 200.

5.1. *Rigid-rigid cavity*

In this case, the fluid flow is generated by buoyancy forces due to the temperature gradients in the liquid resulting from the lateral heating. The calculations were carried out for Grashof numbers ranging from 10^4 to 2.0×10^4, and various values of the Hartmann number, $0 \leqslant Ha \leqslant 200$. In this range of Grashof numbers the flow for $Ha = 0$ is expected to be steady with intense convective rolls (see Roux 1990; Ben Hadid & Roux 1990). Figure 9(*a–d*) shows the streamlines patterns at Hartmann numbers of 0, 5, 10 and 100, respectively. For a zero Hartmann number (figure 9*a*), there is an intense circulation loop in the central region and two smaller ones near the endwalls. As the Hartmann number is increased to 5, the small rolls disappear and the central circulation is seen to spread gradually over the whole cavity. On a further increase in Hartmann number, the streamlines in the central region become more and more horizontal whereas they accumulate near the endwalls indicating the existence of a boundary layer at these walls (figure 9*d*). Boundary layers are also formed adjacent to the horizontal walls of the cavity.

The horizontal and vertical normalized velocity profiles are shown, respectively,

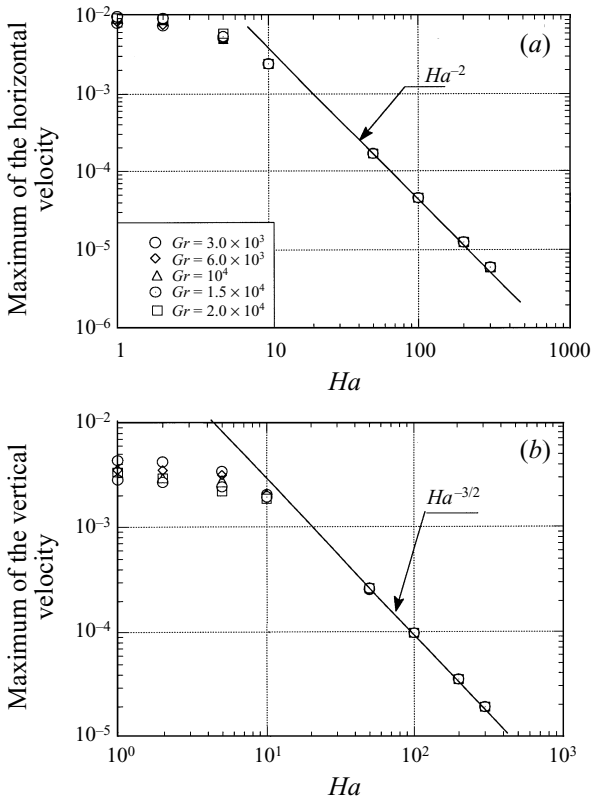

FIGURE 12. Plots of the maxima of the horizontal velocity (*a*) and of the vertical velocity (*b*) as a function of the Hartmann number. The velocities are non-dimensionalized by vGr/H. Results obtained in the rigid–rigid case for various Grashof numbers from $Gr = 3 \times 10^3$ to $Gr = 2 \times 10^4$. For large *Ha*, Ha^{-2} and $Ha^{-3/2}$ variations are depicted respectively for the horizontal and vertical velocity.

in figures 10 and 11. It is clear from figure 10 that the horizontal velocity which was observed to be horizontally invariant at large *Ha* (figure 9) possesses profiles which are more and more linear with respect to the vertical coordinate as *Ha* is increased. The vertical velocity profiles show the progressive disappearance of the vertical velocity in the major part of the cavity except near the endwalls. In these regions, the two small recirculations already mentioned in the analytical calculation (§3.2) are clearly visible.

It is also clear that the use of a magnetic field can strongly decrease the flow intensity, but cannot completely inhibit fluid motions. The plot of the maximum of the velocity as a function of the Hartmann number is displayed in figure 12(*a*, *b*). After an initial transient variation, the curves in log-log coordinates attain an asymptotic linear decrease at *Ha* around 10. Beyond this point the magnetic damping responsible for the great reduction of the convective flow is fully effective. In this domain ($Ha > 10$), u_{max} and w_{max} are shown to fit fairly well respectively the relations (4.3) and (4.4) obtained previously by scaling analysis.

The temperature distribution given in figure 13 shows that convection does not play an important role in the heat transfer which is of conductive type when the Hartmann number is increased over $Ha = 20$. It can be observed that as *Ha* is increased the

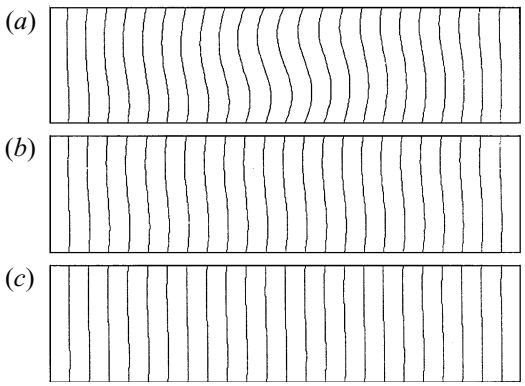

FIGURE 13. Isotherm lines giving the temperature distribution in the cavity. Results obtained in the rigid–rigid case for buoyancy effect ($Gr = 2 \times 10^4$) and (*a*) $Ha = 0$; (*b*) $Ha = 10$; (*c*) $Ha = 20$.

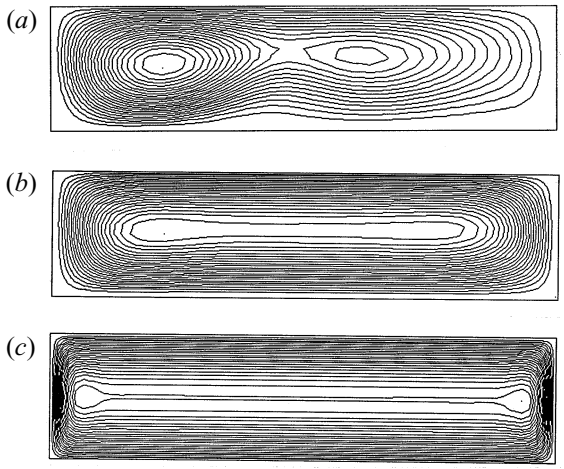

FIGURE 14. Streamlines giving the structure of the flow in the cavity. Results obtained in the rigid–free case for pure buoyancy effect ($Gr = 10^4$, $Re = 0$) and (*a*) $Ha = 0$; (*b*) $Ha = 10$; (*c*) $Ha = 100$.

isotherm-lines which are distorted in the absence of magnetic field (figure 13*a*) become gradually straightlines (see figure 13*c*).

5.2. *Rigid–free cavity*

The calculations of pure buoyancy-driven flow predicted that the primary cell of the circulation is drawn toward the cold wall as the Grashof number is increased, and that for sufficiently high values of Gr, for instance $Gr = 10^4$ (see figure 14*a*), a secondary cell develops. The flow structures displayed in figure 14(*a–c*) for three Hartmann numbers show that with the increase of *Ha* the secondary circulation vanishes and the primary one expands (figure 14*b*). When $Ha = 100$ (figure 14*c*) the circulation is less vigorous but extends over the whole cavity, giving a more and more symmetric flow structure similar to that obtained with rigid walls except that there is no real Hartmann layer near the upper free surface. In fact, as can be seen from equation (3.6), we can consider that we have a weaker type of Hartmann layer which involves a rapid change (exponential variation) in stress to give the no-stress condition at the

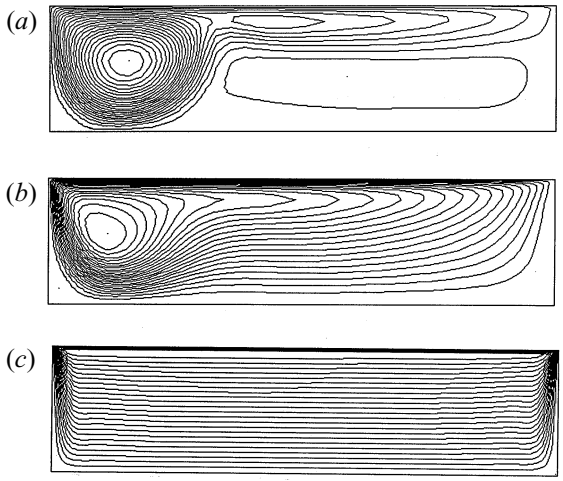

FIGURE 15. As figure 14 but for pure thermocapillary effect ($Gr = 0$, $Re = 10^4$).

free surface. Furthermore, the characteristic behaviour of the two components of the velocity for large values of Ha are similar to those obtained in the rigid–rigid case.

In the pure thermocapillary case the flow structure at $Re = 10^4$ is shown in figure 15(*a–c*) for $Ha = 0$, 10 and 100. In the absence of a magnetic field (figure 15*a*) the flow corresponds to a strong counterclockwise cell with the centre located near the cold wall. At $Ha = 10$ (figure 15*b*), the strength of the flow decreases but the cellular structure persists. Large Hartmann numbers ($Ha = 100$) decrease the flow strength to the point that a single cell stretches to fill the whole cavity so that most of the flow is perpendicular to the field and hence affected by it. The flow becomes more and more antisymmetric with respect to the centre vertical line, and unidirectional over most of the cavity except in the close vicinity of the vertical walls (figure 15*c*). The most vigorous flow is limited to a small region near the free surface (subsurface layer), whereas the returning flow occurs with a constant velocity over almost the whole height of the cavity.

The maximum of the velocity as a function of the Hartmann number is plotted in figure 16 where we can observe that for large values of Ha the maximum of the horizontal velocity, u_{max}, and the maximum of the vertical velocity, w_{max}, satisfy the relations given by scaling analysis, respectively (4.6) and (4.7).

The effect of increasing the strength of the magnetic field in the case of a combined buoyancy and thermocapillary-driven flow is evident in the flow structures shown in figure 17(*a–c*) for three Bond numbers, $Bd = 0.6$, 6 and 60 for a fixed Hartmann number, $Ha = 100$. Examination of these figures shows that the characteristics of the final flow structures depend strongly on Bd. For $Bd = 0.6$ (figure 17*a*) the flow pattern is in a qualitative sense similar to that of the pure thermocapillary case (figure 15*c*), while for $Bd = 60$ (figure 17*c*) the flow pattern compares favourably with that of pure buoyancy-driven flow (figure 14*c*).

5.3. *Comparison with the analytical results*

The previous sections clearly show the large modifications of the flow structure which occur under the action of a strong magnetic field. To illustrate further the characteristics of these flows and verify the analytical approach, we will compare

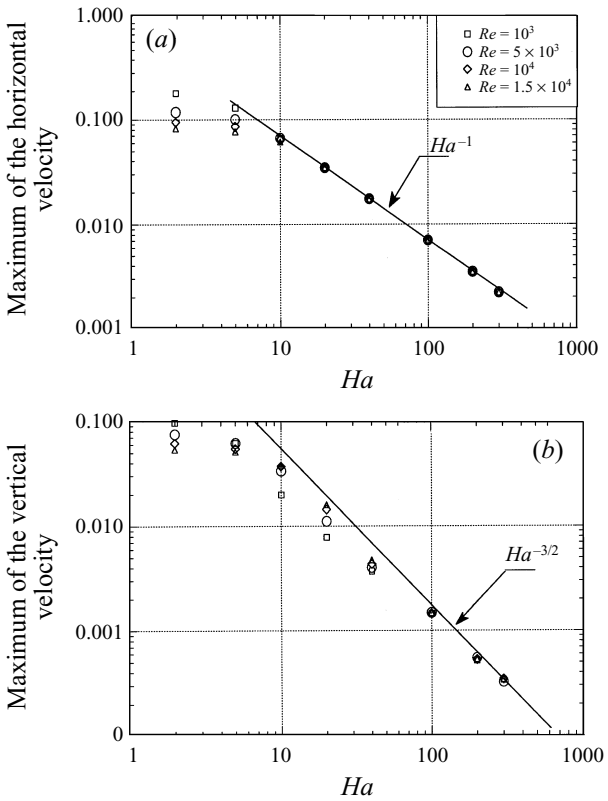

FIGURE 16. Plots of the maxima of the horizontal velocity (*a*) and of the vertical velocity (*b*) as a function of the Hartmann number. The velocities are non-dimensionalized by vRe/H. Results obtained in the thermocapillary case for various Reynolds numbers varying from $Re = 10^3$ to $Re = 1.5 \times 10^4$. For large Ha, Ha^{-1} and $Ha^{-3/2}$ variations are depicted respectively for the horizontal and vertical velocity.

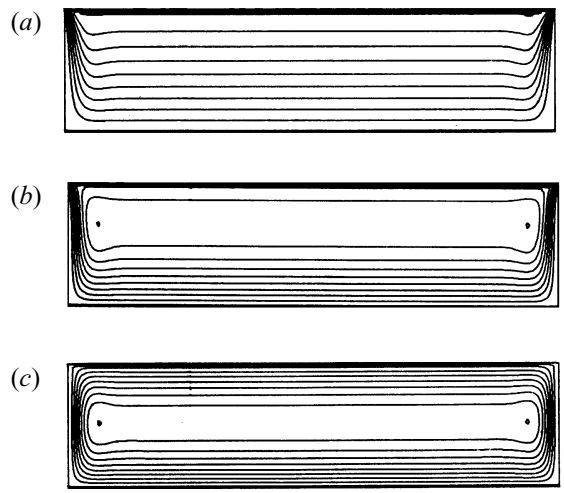

FIGURE 17. Streamlines giving the structure of the flow in the cavity. Results obtained in the rigid–free case for $Ha = 100, Gr = 6 \times 10^3$ with combined buoyancy and thermocapillary effects: (*a*) $Re = 10^4$ ($Bd = 0.6$); (*b*) $Re = 10^3$ ($Bd = 6$); (*c*) $Re = 10^2$ ($Bd = 60$).

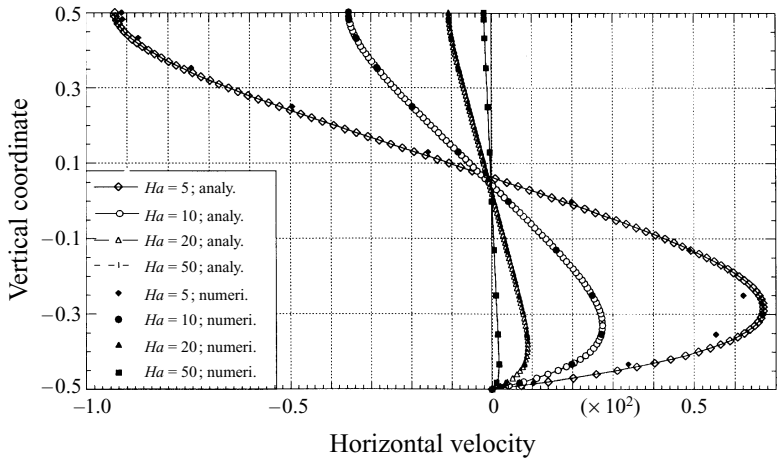

FIGURE 18. Vertical profiles of the horizontal velocity at mid-length of the cavity. Comparison with analytical solutions (3.3) in the rigid–free case for pure buoyancy effect ($Gr = 10^4$, $Re = 0$) and $Ha = 5$, 10, 20 and 50.

characteristic velocity profiles for both buoyancy and thermocapillary cases obtained from the two approaches, i.e. analytical and numerical.

For the central region the comparison will focus on the horizontal velocity profiles at mid-length of the cavity. The analytical profiles are given by equations (3.3), (3.4). In the pure buoyancy-driven flow situation ($Gr = 10^4$), the curves in figure 18 reveal that the analytical velocity profiles are in good agreement with those obtained from the results of the numerical simulations essentially for $Ha \geqslant 10$. For $Ha = 5$ the analytical solution is shown to overestimate the velocity in the lower part of the curve, precisely where the velocity reaches its maximum. In the pure thermocapillary case we observe for $Re = 100$ (figure 19*a*) a very good agreement between the two results for $Ha \geqslant 5$. However, for larger values of the Reynolds number, e.g. $Re = 2 \times 10^3$ (figure 19*b*), a relatively large discrepancy between the two curves is found for $Ha = 5$, whereas for $Ha \geqslant 10$ the analytical curves agree rather well with the numerical ones.

Quantitative comparisons for the turning flow can be made by comparing the vertical velocity at mid-height of the cavity or the surface velocity for cavities with a free surface. The analytical profiles are obtained using equations (3.14) and (3.13), respectively. In the pure buoyancy-driven flow case (figure 20) this comparison demonstrates that the analytical vertical velocity profiles agree with the numerical results rather well for $Ha \geqslant 20$. In the pure thermocapillary case the surface velocity profiles are displayed in figures 21(*a*) and 21(*b*), respectively, for $Re = 10^2$ and 2×10^3. Here we observe that for $Re = 10^2$ and $Ha \geqslant 10$ (figure 21*a*) the curves are close together. But for $Ha = 5$ small differences appear, i.e. the analytical results exhibit a small undershoot for $x < 0.5$, and a small overshoot for $x > 0.8$. For $Re = 2 \times 10^3$ (figure 21*b*) and for $Ha \leqslant 10$, the analytical curves are quite different, essentially near the rigid boundary ($x = 0$). For $Ha = 20$ a small undershoot remains evident for $x < 0.25$, and a rather good agreement is only obtained for $Ha = 30$. Note that all these limiting values of Hartmann number where a good comparison is obtained between the two approaches are in agreement with relations (4.5) and (4.8) derived by scaling analysis. For example, for $Re = 2 \times 10^3$ the value of the Hartmann number sufficient to neglect the inertia terms is (from (4.8)) $Ha \gg 20$. Hence it is not surprising

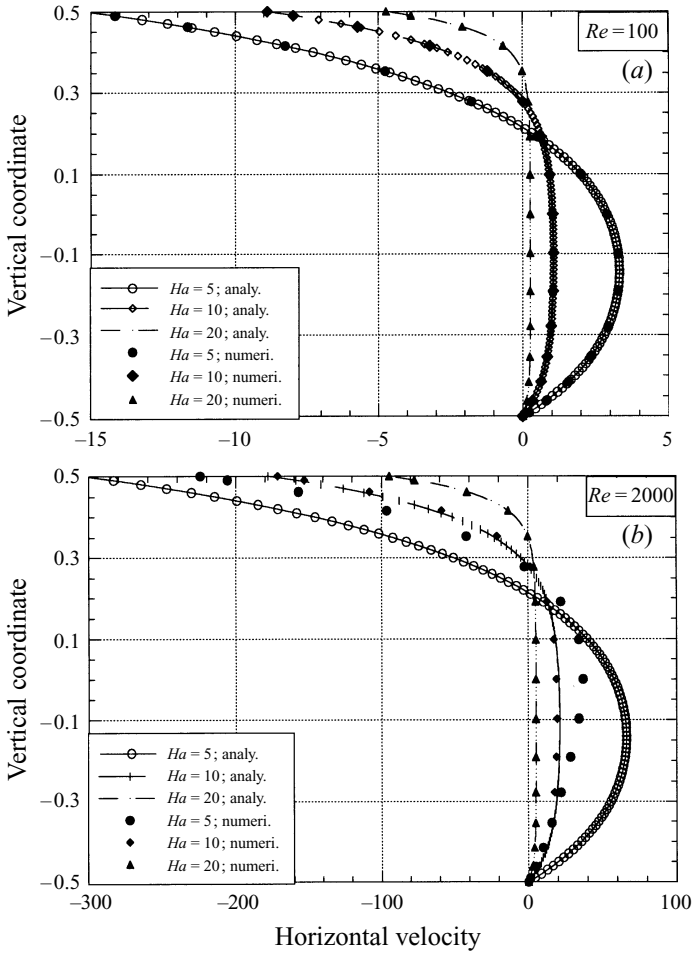

FIGURE 19. Vertical profiles of the horizontal velocity at mid-length of the cavity. Comparison with analytical solutions (3.3) in the rigid–free case for pure thermocapillary effect ($Gr = 0$; (*a*) $Re = 10^2$, (*b*) $Re = 2 \times 10^3$) and $Ha = 5$, 10 and 20.

that some differences in the velocity profiles are observed up to $Ha = 20$ since inertia terms are neglected in the analytical approach.

6. Stability analysis

We consider in this section the stability of buoyancy-driven flow of an electrically conducting fluid in a laterally unbounded layer confined by a solid wall at the bottom and bounded by a stress-free surface ($Re = 0$) at the top. The layer is subjected to a constant horizontal temperature gradient and to a homogeneous vertical magnetic field. We assume that the aspect ratios are large enough and the temperature gradient sufficiently small to obtain a parallel core flow. By increasing the temperature gradient the parallel core flow becomes susceptible to a variety of instabilities and, depending on the Prandtl number, both transverse and longitudinal oscillatory modes are possible (Hart 1972, 1983; Laure & Roux 1987; Roux, Ben Hadid & Laure 1989). The transverse modes correspond to rolls that have axes

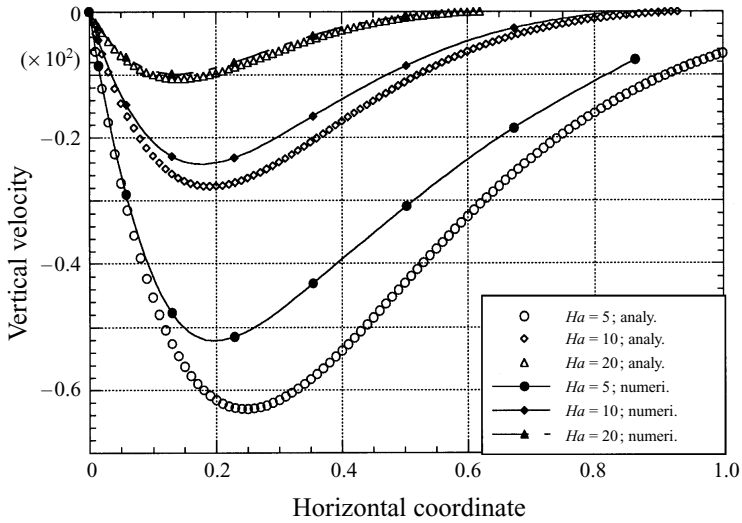

FIGURE 20. Horizontal profiles of the vertical velocity in the turning flow region at mid-height of the cavity. Comparison with analytical solutions (3.14) in the rigid–free case for pure buoyancy effect ($Gr = 10^4$, $Re = 0$) and $Ha = 5$, 10 and 20.

perpendicular to the parallel flow direction and then a two-dimensional flow structure persists, whereas the cells axes for the longitudinal modes are aligned with the parallel flow direction which leads to a global three-dimensional flow structure. For Prandtl numbers less than 0.0045 oscillatory transverse instabilities are the dominant modes, whereas the longitudinal oscillatory modes dominate in the range $0.0045 \leqslant Pr \leqslant 0.41$. More precisely, for the longitudinal instability, travelling waves become the preferred modes for $0.0045 \leqslant Pr \leqslant 0.38$, while standing waves prevail for $0.38 \leqslant Pr \leqslant 0.41$ (Laure & Roux 1987). The linear stability results presented in this section extend those cited above which were obtained without a magnetic field.

In order to analyse the linear stability of the basic state (3.3)–(3.5), the governing equations (2.3-2.7) are linearized with respect to small perturbations ($\boldsymbol{v}'$, p', θ', ϕ'). The dimensionless linearized system of equations to be solved is

$$\nabla \cdot \boldsymbol{v}' = 0, \tag{6.1}$$

$$\frac{\partial \boldsymbol{v}'}{\partial t} + (U_0 \cdot \nabla \boldsymbol{v}' + \boldsymbol{v}' \cdot \nabla U_0) = -\nabla p' + \nabla^2 \boldsymbol{v}' + Gr\theta' \boldsymbol{e}_z + Ha^2(-\nabla \phi' + \boldsymbol{v}' \times \boldsymbol{e}_z) \times \boldsymbol{e}_z, \tag{6.2}$$

$$\frac{\partial \theta'}{\partial t} + (U_0 \cdot \nabla \theta' + \boldsymbol{v}' \cdot \nabla \theta_0) = \frac{1}{Pr} \nabla^2 \theta', \tag{6.3}$$

$$\nabla^2 \phi' = (\nabla \times \boldsymbol{v}') \boldsymbol{e}_z, \tag{6.4}$$

where $U_0 = (u(z), 0, 0)$ and $\theta_0(x, z) = x + Prf(z)$ are obtained from (3.3) and (3.5), respectively. The non-dimensional form of system (6.1)–(6.4) results from the scaling of lengths, velocities and temperature by the reference quantities given in §2.2. The electric potential appearing in equations (6.2) and (6.4) has been scaled by $v|\boldsymbol{B}_0|$. The electric potential boundary conditions associated with equation (6.4) are

$$\left.\frac{\partial \phi'}{\partial z}\right|_{z=-0.5} = \left.\frac{\partial \phi'}{\partial z}\right|_{z=0.5} = 0, \tag{6.5}$$

corresponding to electrically insulated horizontal boundaries.

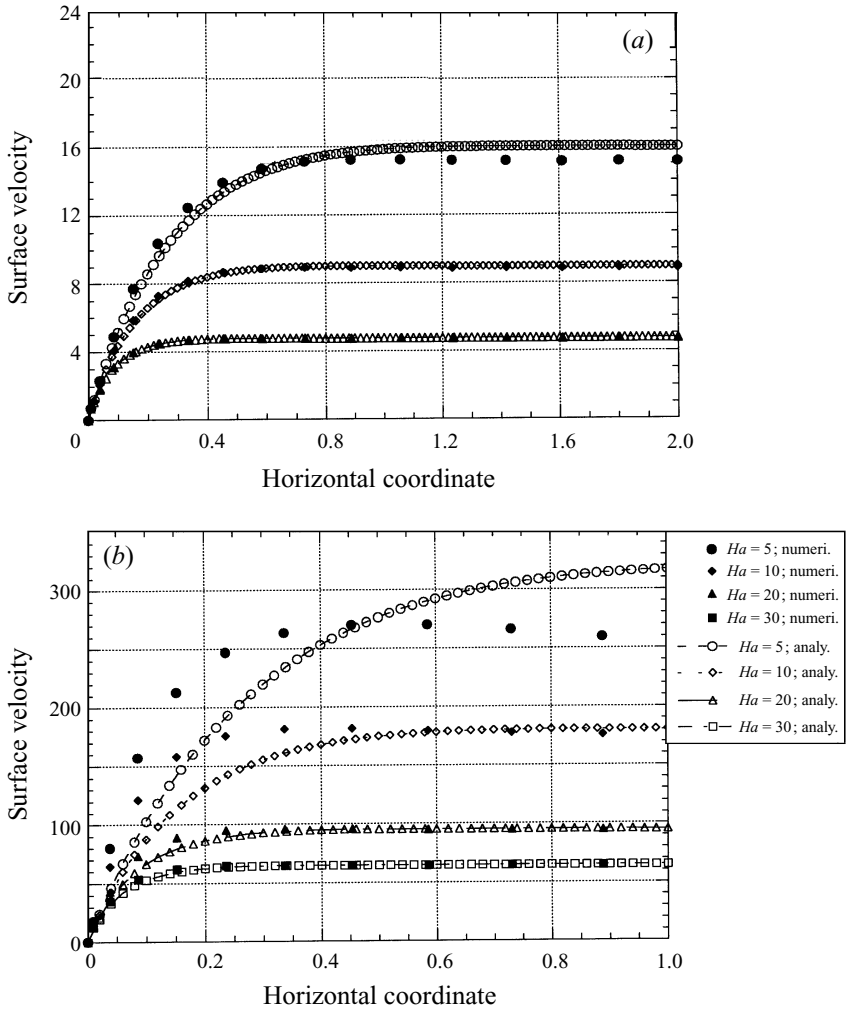

FIGURE 21. Horizontal surface velocity in the turning flow region. Comparison with analytical solutions (3.13) in the rigid–free case for pure thermocapillary effect ($Gr = 0$; (*a*) $Re = 10^2$, (*b*) $Re = 2 \times 10^3$) and several values of the Hartmann number.

The perturbations can be written in normal modes of the form

$$\boldsymbol{v}'(x, y, z) = \boldsymbol{v}'(z)\mathrm{e}^{\mathrm{i}(h_x x + h_y y)+\omega t}, \quad p'(x, y, z) = p'(z)\mathrm{e}^{\mathrm{i}(h_x x + h_y y)+\omega t},$$

$$\theta'(x, y, z) = \theta'(z)\mathrm{e}^{\mathrm{i}(h_x x + h_y y)+\omega t}, \quad \phi'(x, y, z) = \phi'(z)\mathrm{e}^{\mathrm{i}(h_x x + h_y y)+\omega t},$$

which leads to an eigenvalue problem. The parameters h_x, h_y are real wavenumbers in the longitudinal, x, and transverse, y, directions, respectively, and $\omega = \omega_r + \mathrm{i}\,\omega_i$ is a complex eigenvalue, the real part of which being an amplification rate and the imaginary part an oscillatory frequency. According to the linear theory, the flow is stable if, for given values of the governing parameters, e.g. *Pr*, *Gr* and *Ha*, all the eigenvalues have a negative amplification factor ω_r for all values of h_x and h_y. The unstable case corresponds to the situation where, for some values of h_x and h_y, at least one eigenvalue has a positive amplification rate. The state for which the largest amplification rate ω_r is zero is called the state of neutral stability.

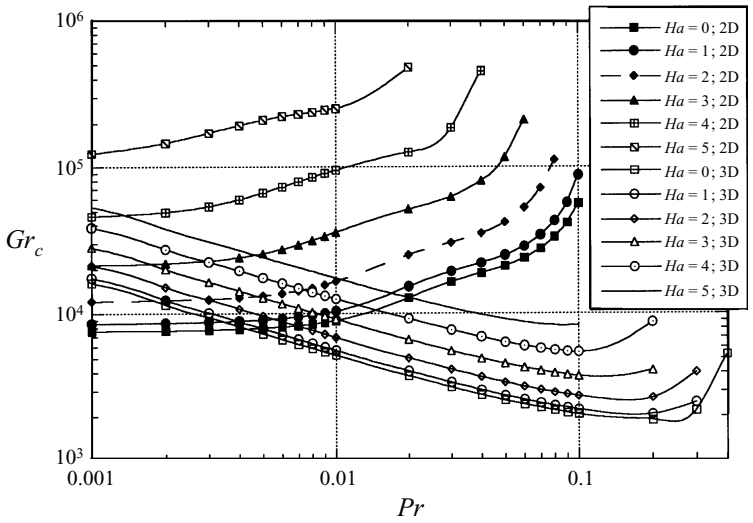

FIGURE 22. Neutral stability curves in the pure buoyancy case with magnetic effect. The critical Grashof number Gr_c is given as a function of Prandtl number Pr for several values of the Hartmann number Ha (from 0 to 5). Two types of curves are obtained corresponding respectively to transverse oscillating modes (two-dimensional structures) and to longitudinal oscillating modes (three-dimensional structures).

The numerical procedure is based on a Tau-method which uses Chebyshev polynomials as trial functions. In the present study we used 20 polynomials which are found sufficient to give grid-free results. The discretized system results in a generalized algebraic eigenvalue problem $\boldsymbol{A}W = \lambda \boldsymbol{B}W$, where $\boldsymbol{A}$ and $\boldsymbol{B}$ are complex matrices. The problem is then solved using the EIGZC routine from the IMSL library. In this routine the eigenvectors are normalized so that the largest component has absolute value 1. The details of the method may be found in Laure (1987).

Our aim is to study the effect of a vertical magnetic field on the stability characteristics. The curves showing the evolution of the critical Grashof number, Gr_c, as a function of the Prandtl number for several Hartmann number values are displayed in figure 22 for thermally insulated horizontal boundaries (denoted the insulated case). The global dynamical behaviour for $0.001 \leqslant Pr \leqslant 0.3$ and $Ha \leqslant 5$ may be described by the two types of curves mentioned above: the first type corresponds to transverse oscillatory modes ($h_x \neq 0$, $h_y = 0$) and prevails for $Pr \leqslant Pr_t$, and the second to longitudinal oscillatory modes ($h_y \neq 0$, h_x very small or zero) and occurs for $Pr > Pr_t$. Here Pr_t is the value of the Prandtl number at which the crossover between the transverse and longitudinal modes occurs. From figure 22 it is evident for both modes that at a given value of Pr the critical Grashof number Gr_c is an increasing function of Ha, indicating the stabilizing influence of the magnetic field. This stabilizing effect is seen to be more effective for the transverse modes, as the curves in that case shift to a larger Grashof number than the curves corresponding to the longitudinal modes. As a result, Pr_t is moved towards smaller values and the range of Prandtl number over which the transverse modes prevail shrinks until it finally disappears for $Ha \geqslant 5$ in the range of Pr studied. For this domain of Ha, the longitudinal oscillatory mode corresponds then to the first instability in the range $0.001 \leqslant Pr \leqslant 0.3$, indicating that, in a laboratory experiment, longitudinal rolls will be the expected outcome. From figure 22, it is also apparent that the stabilizing effect of increasing Ha in the case

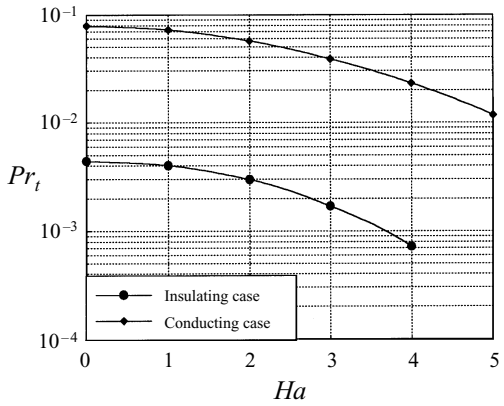

FIGURE 23. Variation with Ha of Pr_t which is the value of the Prandtl number corresponding to the transition between transverse and longitudinal modes. Buoyancy-driven flow case in the rigid–free cavity and for two thermal boundary conditions.

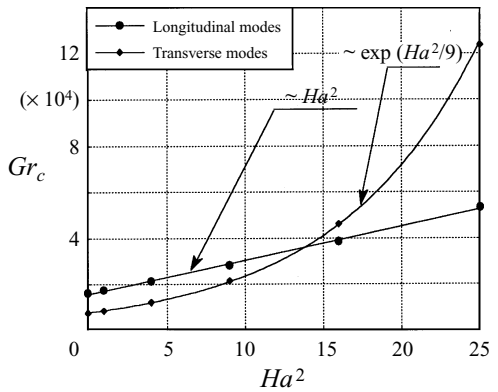

FIGURE 24. Neutral stability curves in the pure buoyancy case with magnetic effect. The critical Grashof number Gr_c is given as a function of Ha^2 for $Pr = 0.001$. The evolution is in Ha^2 for the transverse modes and in $\exp(Ha^2/9)$ for the longitudinal modes.

of the longitudinal modes causes the point at which the Grashof number attains its minimum to move towards smaller values of Pr. We have not investigated the flow for $Ha > 5$, owing to the slow convergence of the series approximations because of the very large values of the critical Grashof number.

More generally, the evolution of the marginal states with regard to the Prandtl number remains qualitatively unchanged when the vertical magnetic field is applied: an increase of Pr is always destabilizing for the longitudinal oscillating modes and stabilizing for the transverse oscillating modes. Moreover, in the limiting case of vanishing Hartmann number, the curves converge to those obtained by Laure & Roux (1987) without a magnetic field.

The curves of Pr_t as a function of the Hartmann number Ha which are displayed in figure 23 show precisely the decrease of Pr_t with increasing Ha for both types of thermal boundary conditions.

Without loss of generality, figure 24 gives an example for the dependence of Gr_c on the Hartmann number for $Pr = 0.001$. The stability curves for the transverse modes show exponentially increasing values of Gr_c with Ha, an evolution much faster than

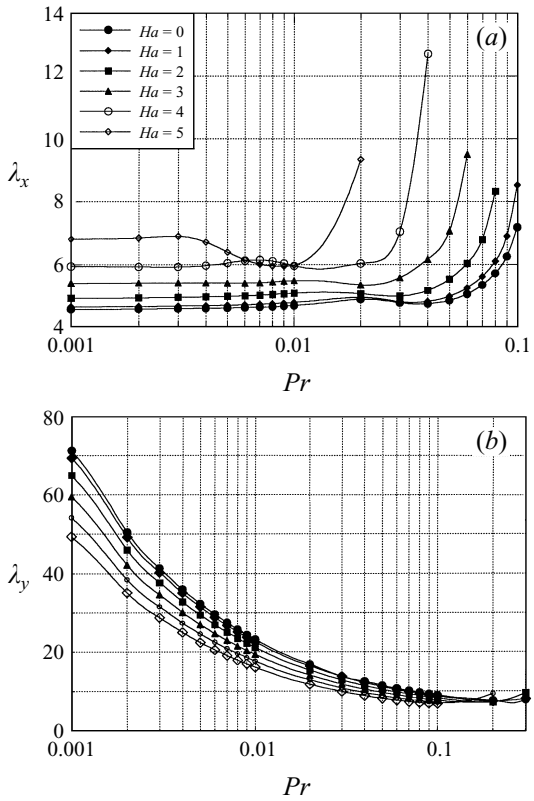

FIGURE 25. Variation with Pr of the wavelength of the neutral modes for several values of the Hartmann number: (a) transverse modes (λ_x); (b) longitudinal modes (λ_y).

for the longitudinal modes. In fact, from the results it is possible to derive for each mode a simple relationship giving the dependence of Gr_c on Ha. This relationship may be written in the form $Gr_c \sim \exp(Ha^2/9)$ for the transverse modes and $Gr_c \sim Ha^2$ for the longitudinal modes. More general relationships may be found by including the effect of Pr: $Gr_c \sim Ha^2 Pr^{-1/2}$ for the longitudinal modes, valid for $0.001 \leqslant Pr \leqslant 0.1$, and again $Gr_c \sim \exp(Ha^2/9)$ for the transverse modes, valid in the limit of very small Pr. Note that the Ha^2 dependence of the critical Grashof number was pointed out in the experimental investigations of Hurle *et al.* (1974).

We display in figure 25 the curves of critical wavelength as a function of the Prandtl number for the transverse ($\lambda_x = 2\pi/h_x$) and longitudinal ($\lambda_y = 2\pi/h_y$) oscillatory modes. Examination of these curves reveals that for $Pr < 0.02$, the variation of λ_x with Pr is relatively small, but it becomes more important for $Pr > 0.02$. For λ_y a rapid decrease is observed in the range $Pr < 0.1$. For the longitudinal modes, an increase of Ha up to 5 produces relatively moderate effects on λ_y which goes down as Ha is increased. In contrast, for the transverse modes, the curves for λ_x are shifted up and appear to be more sensitive to the effect of the magnetic field. This feature corresponds to an increase of the size of the secondary transverse cells as Ha increases. It is qualitatively contrary to what is observed in the Rayleigh–Bénard problem (see Chandrasekhar 1961), where the cells tend to become more narrow as the strength of the magnetic field is increased.

Typical characteristics of the flow at the marginal state for the transverse and

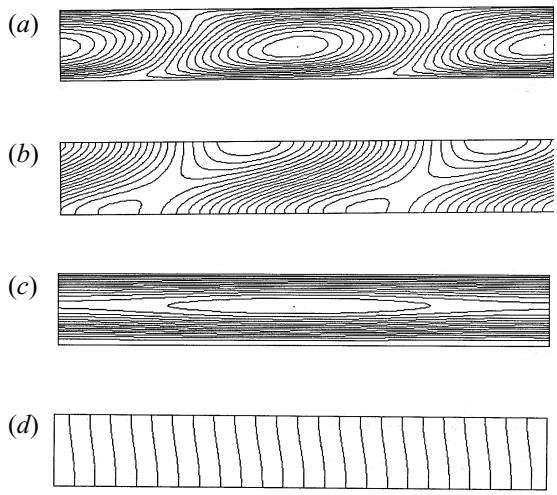

FIGURE 26. Flow characteristics for the transverse mode corresponding to a two-dimensional structure in the (x, z)-plane. Streamlines and isotherms for the perturbation (respectively, (a) and (b)) and for the global solution (respectively, (c) and (d)) are given for the marginal state at $Pr = 0.001$ and $Ha = 5$.

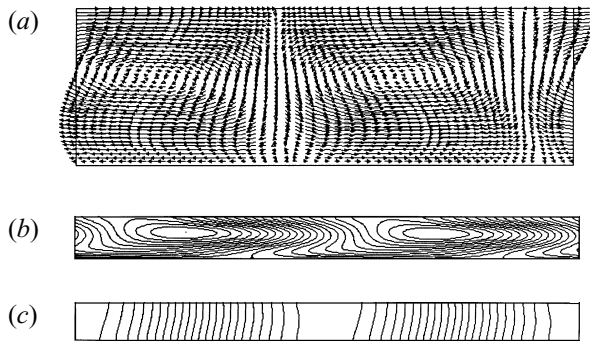

FIGURE 27. Flow characteristics for the three-dimensional longitudinal mode given in the (y, z) plane. The velocity field projection (a), the iso-lines for the longitudinal velocity u' (b) and the isotherms (c) are given for the perturbation at marginal state at $Pr = 0.02$ and $Ha = 5$. The relative height of the cavity is increased for the velocity field representation.

longitudinal modes are given in figures 26 and 27, respectively. For the graphic representation of the global solution, we superpose on the base flow ϵ times the perturbation which corresponds to the more unstable eigenvector ($\epsilon = 0.001$). For the transverse modes (two-dimensional structure in the (x, z)-plane), the streamlines and isotherms of both the perturbation and the global solution are presented for $Pr = 0.001$ and $Ha = 5$. The results resemble those obtained for $Ha = 0$. The main difference is the increase of the wavelength of the perturbation but modifications are also observed in the temperature perturbation. Results for the longitudinal modes (three-dimensional structure) are given in the (y, z)-plane, the main plane for the perturbation as h_x is very small or zero, for $Pr = 0.02$ (corresponding to molten gallium) and $Ha = 5$. In figure 27 are displayed the perturbation characteristics, namely the projection of the velocity field (a) (with an increase of the height of the

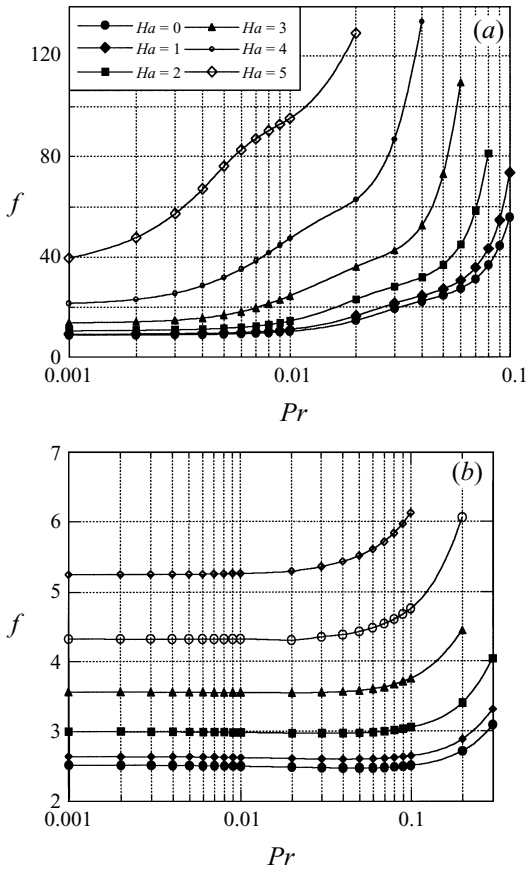

FIGURE 28. Variation with Pr of the frequency of the neutral modes for several values of the Hartmann number: (*a*) transverse modes; (*b*) longitudinal modes.

cavity for a better presentation), the iso-longitudinal velocity u' (*b*) and the isotherms (*c*).

The curves of the frequency of oscillations ($f = \omega_i/2\pi$) displayed in figure 28 reveal essentially that an increase of Ha always produces an increase of the frequency. The variation with respect to Pr is similar to the case without a magnetic field: relatively constant for the longitudinal modes and increasing with Pr for the transverse modes. Furthermore, this growth of the frequency with Ha may be related to the increase of Gr_c due to the stabilizing effects of the magnetic field.

The electric potential is found to be constant for the transverse modes, and has no influence on the stability thresholds. For the longitudinal modes, it shows variations in the (y, z)-plane which are displayed in figure 29(*a*). The creation of an electric potential is connected to transverse variations of u' (the longitudinal velocity perturbation given in figure 27*b*). The perturbation current in this plane which corresponds to

$$J'_y = -\frac{\partial \phi'}{\partial y}(y,z) - u'(y,z), \quad J'_z = -\frac{\partial \phi'}{\partial z}(y,z),$$

and includes the directly induced current and the potential one is illustrated in figure

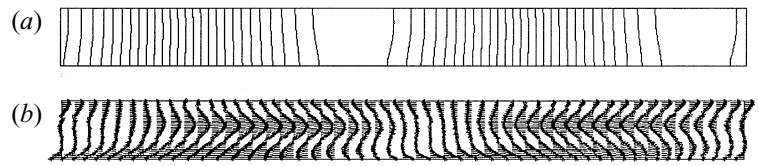

FIGURE 29. Electric characteristics for the three-dimensional longitudinal mode given in the (y,z)-plane. The iso-lines for the electric potential (a) and the electric current projection (b) are given for the perturbation at marginal state at $Pr = 0.02$ and $Ha = 5$.

29(b). The global current in the cavity is in fact given by

$$J'_x = v'(y,z), \quad J'_y = -\frac{\partial \phi'}{\partial y}(y,z) - (u'(y,z) + u(z)), \quad J'_z = -\frac{\partial \phi'}{\partial z}(y,z),$$

but the two new terms are conservative. The effect of the electric potential, as seen in the (y,z)-plane, is thus to slow down the directly induced current and to allow counter circulation along the boundaries (mainly the no-slip bottom boundary) for the conservation of the current. The potential will then decrease the stabilizing effect generated by the directly induced current. This is confirmed by the fact that for the longitudinal modes the instability thresholds increase if we neglect the potential effect.

The results obtained with thermally conducting horizontal boundaries reveal the same qualitative influence of the Hartmann number on the main characteristics of the transverse and longitudinal oscillatory modes. The main differences are connected with the influence of Pr and were already observed without a magnetic field: first the value of Pr_t is larger (see figure 23) and then the variation with Pr of the wavelength and of the frequency of the longitudinal modes are changed.

Some general comments on the stability analyses can be made. The action of the magnetic field on the stability characteristics is twofold: it appears in the analytical velocity and temperature equations for the basic state as well as in the linearized governing equation (6.2) in the Lorentz force term. It is established from the foregoing results (see §5) that the asymptotic behaviour of the velocity (with a Ha^{-2} dependence) occurs only for $Ha > 10$. As all our results in the stability analysis are obtained for $Ha \leqslant 5$, this may suggest that the stabilizing effect is more effective in the Lorentz force which is directly proportional to Ha^2. Concerning the different variation with Ha of the transverse and longitudinal modes, it may be noted that the transverse modes are of dynamical origin (asymptotic behaviour for $Pr = 0$ and increase of the thresholds as Pr increases) whereas the longitudinal modes are of thermal origin (increase of the thresholds as Pr decreases). Moreover, the decrease of wavelength as Ha is increased is observed for our longitudinal modes as well as in the Rayleigh–Bénard situation, both corresponding to instabilities of thermal origin.

7. Conclusions

We investigated the effect of a constant magnetic field on the flow states in a differentially heated horizontal Bridgman cavity. We derived analytical solutions for the horizontal velocity in the central region and for the two components of the velocity in the turning flow region. We also performed numerical simulations for a cavity with a moderate aspect ratio $A = 4$. One obvious finding is that for increasing values of the Hartmann number, i.e. for increasing strength of the magnetic field, the intensity of the convective flow decreases and is followed by a progressive change of the overall struc-

ture of the flow. When $Ha > 10$ the overall character of the flow is greatly modified. Thus, several noteworthy features are: (i) by increasing the Hartmann number the velocity decreases and has an asymptotic behaviour which is found to follow a power law; (ii) the flow becomes more and more unidirectional in the central region and boundary layers develop in the vicinity of the rigid walls; (iii) the characteristics of the final flow structure are found to depend on the type of driving force. For example, the typical velocity profile in the core is linear with respect to the vertical coordinate in the buoyancy-driven flow case whereas it is constant for the thermocapillary-driven flow.

The analytical velocity profiles obtained with some simplifying assumptions agree well with the corresponding numerical velocity profiles for certain values of the Hartmann number. This good agreement implies that in a certain range of Ha the flow in a finite cavity may be accurately modelled by a simplified analytical model. This range is found to correspond to $Ha^3 \gg Gr$ for the pure buoyancy-driven flow and to $Ha^{5/2} \gg Re$ for the pure thermocapillary-driven flow.

The stability of natural convection in a laterally unbounded horizontal layer with the upper free surface subjected to a horizontal temperature gradient is also considered herein when a constant, vertical magnetic field is applied. The critical Grashof number Gr_c for the onset of instability is determined as a function of the Prandtl number up to $Ha = 5$. We have found that Gr_c increases linearly with the square of the Hartmann number for the longitudinal modes and exponentially for the transverse modes. This result confirms the stabilizing effect of the magnetic field, already observed in the experiments of Hurle *et al.* (1974) and Davoust *et al.* (1994). Furthermore, since the stabilizing effect is more effective on the transverse oscillating modes, the longitudinal oscillating modes (which generate a three-dimensional flow structure) become for $Ha \geqslant 5$ the preferred ones over the entire range of investigated Prandtl number $0.001 \leqslant Pr \leqslant 0.3$. Consequently, for large Hartmann number three-dimensional simulations become necessary in order to understand the interaction between the magnetic field and the flow field. Moreover, in real situations, the presence of lateral walls, which was not taken into account here, may also introduce important three-dimensional modifications in the flow structure. This three-dimensional aspect of the problem will be treated in Part 2 (Ben Hadid & Henry 1997).

We wish to thank Professor R. Moreau and Dr T. Alboussière from MADYLAM and Dr J. P. Garandet from CEN Grenoble for fruitful discussions. The authors also wish to thank Dr P. Laure from I.N.L Nice for helpful suggestions in the stability analysis part. They particularly acknowledge Dr B. Roux from I.M.F. Marseille and Professor R. L. Sani from the University of Colorado for valuable advices. This work is supported by the "Centre National des Etudes Spatiales" (Division Microgravité Fondamentale et Appliquée). The calculations were carried out on a Cray YMP C98 computer with the support of the CNRS through the "Institut du Développement et des Ressources en Informatique Scientifique".

Appendix

If we put the expansion (3.12) in equation (3.11), we get

$$\sum_{j=0}^{\infty}(V_j^{(4)} - 2\alpha_j^2 V_j^{(2)} + \alpha_j^4 V_j + Ha^2\alpha_j^2 V_j)\cos(\alpha_j z)$$

$$+\sum_{k=0}^{\infty}(W_k^{(4)} - 2\gamma_k^2 W_k^{(2)} + \gamma_k^4 W_k + Ha^2\gamma_k^2 W_k)\sin(\gamma_k z) + Ha^2 Re\, z + Ha^2 \tfrac{1}{2} Re = Gr. \quad \text{(A 1)}$$

We need then to express the functions 1, z, z^2 and z^3 in the orthogonal basis of the sine and cosine functions. We get

$$1 = \sum_{j=0}^{\infty} \frac{4(-1)^j}{\alpha_j} \cos(\alpha_j z), \qquad (z^2 - 4) = \sum_{j=0}^{\infty} \frac{-8(-1)^j}{\alpha_j^3} \cos(\alpha_j z), \tag{A 2}$$

$$z = \sum_{k=0}^{\infty} \frac{2(-1)^k}{\gamma_k} \sin(\gamma_k z), \qquad (z^3 - \tfrac{1}{4}z) = \sum_{k=0}^{\infty} \frac{-12(-1)^k}{\gamma_k^3} \sin(\gamma_k z). \tag{A 3}$$

By replacing $Ha^2 Re\, z$ and $(Ha^2\, Re/2 - Gr)$ by their expansions and taking into account the orthogonality of the sine and cosine functions, we obtain

$$\forall j, \qquad V_j^{(4)} - 2\alpha_j^2 V_j^{(2)} + (\alpha_j^4 + Ha^2\alpha_j^2) V_j = g_j, \tag{A 4}$$

and

$$\forall k, \qquad W_k^{(4)} - 2\gamma_k^2 W_k^{(2)} + (\gamma_k^4 + Ha^2\gamma_k^2) W_k = h_k, \tag{A 5}$$

with

$$g_j = (-Ha^2 \tfrac{1}{2} Re + Gr) \frac{4(-1)^j}{\alpha_j} \quad \text{and} \quad h_k = -Ha^2 Re \frac{2(-1)^k}{\gamma_k}.$$

These two equations have the same form. Let us consider the first one. Its characteristic equation is

$$m^4 - 2\alpha_j^2 m^2 + (\alpha_j^4 + Ha^2\alpha_j^2) = 0$$

and the solution is of the form $m = \pm a_j \pm \mathrm{i} b_j$ with

$$a_j = \frac{1}{\sqrt{2}} \Big(\alpha_j^2 + \alpha_j (Ha^2 + \alpha_j^2)^{1/2} \Big)^{1/2} \quad \text{and} \quad b_j = \frac{1}{\sqrt{2}} \Big(-\alpha_j^2 + \alpha_j (Ha^2 + \alpha_j^2)^{1/2} \Big)^{1/2}.$$

A particular solution of the global equation is $g_j/(\alpha_j^4 + Ha^2\alpha_j^2)$. We can then write the global solution as

$$V_j(x) = \lambda_j \mathrm{e}^{-a_j x} \cos(b_j x) + \mu_j \mathrm{e}^{-a_j x} \sin(b_j x) + \lambda_j' \mathrm{e}^{a_j x} \cos(b_j x) + \mu_j' \mathrm{e}^{a_j x} \sin(b_j x) + \frac{g_j}{\alpha_j^4 + Ha^2\alpha_j^2}.$$

As V_j must be finite as x tends towards infinity, λ_j' and μ_j' must be zero. We have then for V_j and W_k

$$V_j(x) = \lambda_j \mathrm{e}^{-a_j x} \cos(b_j x) + \mu_j \mathrm{e}^{-a_j x} \sin(b_j x) + \frac{g_j}{\alpha_j^4 + Ha^2\alpha_j^2}, \tag{A 6}$$

and

$$W_k(x) = \nu_k \mathrm{e}^{-c_k x} \cos(d_k x) + \pi_k \mathrm{e}^{-c_k x} \sin(d_k x) + \frac{h_k}{\gamma_k^4 + Ha^2\gamma_k^2}, \tag{A 7}$$

with c_k and d_k defined as a_j and b_j. The solution is then obtained from (3.12) with the expressions for V_j and W_k given above.

We must then verify the boundary conditions at $x = 0$: $\psi = 0$ and $(\partial\psi/\partial x) = 0$. For that, we need to know the expansion of the polynome P on the basis. By using expressions (A 2)–(A 3), we can write

$$\psi = \sum_{j=0}^{\infty} (V_j(x) - V_{j0}) \cos(\alpha_j z) + \sum_{k=0}^{\infty} (W_k(x) - W_{k0}) \sin(\gamma_k z),$$

with

$$V_{j0} = -Re\frac{2(-1)^j}{\alpha_j^3} \quad \text{and} \quad W_{k0} = -Re\frac{2(-1)^k}{\gamma_k^3}.$$

The boundary conditions are then

$$\forall j, \qquad V_j(x=0) = V_{j0} \quad \text{and} \quad V_j'(x=0) = 0,$$

and

$$\forall k, \qquad W_k(x=0) = W_{k0} \quad \text{and} \quad W_k'(x=0) = 0,$$

which gives

$$\lambda_j = V_{j0} - \frac{g_j}{\alpha_j^4 + Ha^2\alpha_j^2}, \quad \mu_j = \frac{a_j}{b_j}\lambda_j,$$

and

$$\nu_k = W_{k0} - \frac{h_k}{\gamma_k^4 + Ha^2\gamma_k^2}, \quad \pi_k = \frac{c_k}{d_k}\nu_k.$$

REFERENCES

Alboussière, T., Garandet, J. P. & Moreau, R. 1993 Buoyancy-driven convection with a uniform magnetic field. Part 1. Asymptotic analysis. *J. Fluid Mech.* **253**, 545–563.

Baumgartl, J. & Müller, G. 1992 Calculation of the effects of magnetic field damping on fluid flow – Comparison of magnetohydrodynamic models of different complexity. In *Proc. VIIIth European Symposium on Materials and Fluid Sciences in Microgravity* (ESA SP-333), pp. 161–164. ESA Publ. Division c/o ESTEC, Noordwijk, The Netherlands.

Ben Hadid, H. 1989 Etude numérique des mouvements convectifs au sein des fluides de faible nombre de Prandtl. Thèse de Doctorat d'Etat, University of Aix-Marseille II, France.

Ben Hadid, H. & Henry, D. 1997 Numerical study of convection in the horizontal Bridgman configuration under the action of a constant magnetic field. Part 2. Three-dimensional flow. *J. Fluid Mech.* **333**, 57–83.

Ben Hadid, H. & Roux, B. 1990 Thermocapillary convection in long horizontal layers of low-Prandtl-number melts subject to a horizontal temperature gradient. *J. Fluid Mech.* **221**, 77–103.

Ben Hadid, H. & Roux, B. 1992 Buoyancy- and thermocapillary-driven flows in differentially heated cavities for low-Prandtl-number fluids. *J. Fluid Mech.* **235**, 1–36.

Carruthers, J. R. 1977 Thermal convection instabilities relevant to crystal growth from liquids. In *Preparation and Properties of Solid state Materials* (ed. W. R. Wilcox & R. A. Lefever), Vol. 3. M. Dekker.

Chandrasekhar, S. 1961 *Hydrodynamic and Hydromagnetic Stability*. Clarendon Press.

Davoust, L., Moreau, R., Bolcato, R., Alboussière, T., Neubrand, A. C. & Garandet, J. P. 1994 Influence of a vertical magnetic field on convection in the horizontal Bridgman crystal growth configuration. In *Proc. 2nd Intl Conf. on Energy Transfer in Magnetohydrodynamic flows, Aussois, France*, Vol. 1, pp. 15–26.

Garandet, J. P., Alboussière, T. & Moreau, R. 1992 Buoyancy driven convection in a rectangular enclosure with a transverse magnetic field. *Intl J. Heat Mass Transfer* **35**, 741–748.

Hart, J. E. 1972 Stability of thin non-rotating Hadley circulations. *J. Atmos. Sci.* **29**, 687–697.

Hart, J. E. 1983 A note on the stability of low-Prandtl-number Hadley circulations. *J. Fluid Mech.* **132**, 271–281.

Hung, M. C. & Andereck, C. D. 1988 Transitions in convection driven by a horizontal temperature gradient. *Phys. Lett.* A **132**, 253–258.

Hung, M. C. & Andereck, C. D. 1990 Subharmonic transitions in convection in a moderately shallow cavity. In *Numerical Simulation of Oscillatory Convection in low-Pr Fluids* (ed. B. Roux). Notes on Numerical Fluid Mechanics, vol. 27, pp. 338–343. Vieweg.

Hurle, D. T. J., Jakeman, E. & Johnson, C. P. 1974 Convective temperature oscillations in molten gallium. *J. Fluid Mech.* **64**, 565–576.

Kaddeche, S., Ben Hadid, H. & Henry, D. 1994 Macrosegregation and convection in the horizontal Bridgman configuration. I. Dilute alloys. *J. Cryst. Growth* **135**, 341–353.

Kim, D. H., Adornato, P. M. & Brown, R. A. 1988 Effect of vertical magnetic field on convection and segregation in vertical Bridgman crystal growth. *J. Cryst. Growth* **89**, 339–356.

Laure, P. 1987 Etude des mouvements de convection dans une cavité rectangulaire soumise à un gradient de température horizontal. *J. Méc. Théor. Appl.* **6**, 351–382.

Laure, P. & Roux, B. 1987 Synthèse des résultats obtenus par l'étude de stabilité des mouvements de convection dans une cavité horizontale de grande extension. *C. R. Acad. Sci. Paris* **305**, 1137–1143.

Motakef, S. 1990 Magnetic field elimination of convective interference with segregation during vertical-Bridgman growth of doped semiconductors. *J. Cryst. Growth* **104**, 833–850.

Oreper, G. M. & Szekely, J. 1983 The effect of an externally imposed magnetic field on buoyancy driven flow in a rectangular cavity. *J. Cryst. Growth* **64**, 505–515.

Oreper, G. M. & Szekely, J. 1984 The effect of a magnetic field on transport phenomena in a Bridgman-Stockbarger crystal growth. *J. Cryst. Growth* **67**, 405–419.

Ozoe, H. & Okada, K. 1989 The effect of the direction of the external magnetic field on the three-dimensional natural convection in a cubical enclosure. *Intl J. Heat Mass Transfer* **32**, 1939–1954.

Pratte, J. M. & Hart, J. E. 1990 Endwall driven, low Prandtl number convection in a shallow rectangular cavity. *J. Cryst. Growth* **102**, 54–68.

Roux, B. (Ed.) 1990 *GAMM Workshop : Numerical Simulation of Oscillatory Convection in low-Pr Fluids*. Notes on Numerical Fluid Mechanics, vol. 27. Vieweg.

Roux, B., Bontoux, P., Loc, T. P. & Daube, O. 1979 *Optimisation of Hermitian Methods for N. S. Equations in Vorticity and Stream Function Formulation*. Lecture Notes in Mathematics, vol. 771, pp. 450–468. Springer.

Roux, B., Ben Hadid, H. & Laure, P. 1989 Hydrodynamical regimes in metallic melts subject to a horizontal temperature gradient. *Eur. J. Mech.* B/*Fluids* **8**, 375–396.

Series, R. W. & Hurle, D. T. J. 1991 The use of magnetic fields in semiconductor crystal growth. *J. Cryst. Growth* **113**, 305–328.

Thompson, J. F., Thames, F. C. & Mastin, C. W. 1974 Automatic numerical generation of a body-fitted curvilinear system. *J. Comput. Phys.* **15**, 299–319.